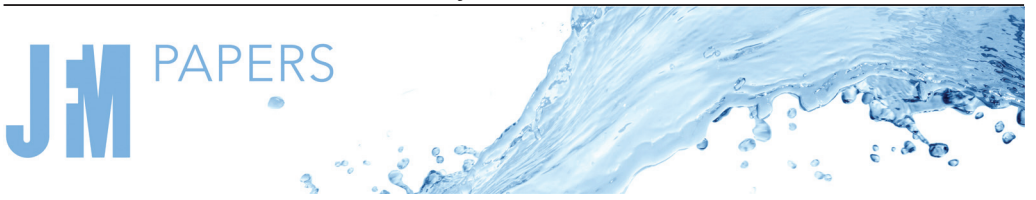
J. Fluid Mech. (2022), *vol*. 943, A22, doi:10.1017/jfm.2022.415



Analytic adjoint solutions for the 2-D incompressible Euler equations using the Green's function approach

Carlos Lozano[1] **and Jorge Ponsin**[1],†

[1]Computational Aerodynamics, National Institute of Aerospace Technology (INTA), Carretera de Ajalvir, Km 4, 28850 Torrejon de Ardoz, Spain

(Received 21 September 2021; revised 24 March 2022; accepted 3 May 2022)

The Green's function approach of Giles and Pierce (*J. Fluid Mech.*, vol. 426, 2001, pp. 327–345) is used to build the lift and drag based analytic adjoint solutions for the two-dimensional incompressible Euler equations around irrotational base flows. The drag-based adjoint solution turns out to have a very simple closed form in terms of the flow variables and is smooth throughout the flow domain, while the lift-based solution is singular at rear stagnation points and sharp trailing edges owing to the Kutta condition. This singularity is propagated to the whole dividing streamline (which includes the incoming stagnation streamline and the wall) upstream of the rear singularity (trailing edge or rear stagnation point) by the sensitivity of the Kutta condition to changes in the stagnation pressure.

Key words: aerodynamics

1. Introduction

The aim of this paper is to apply the program developed by Giles & Pierce (1997, 1998, 2001) to the 2-D incompressible adjoint Euler equations to obtain the analytic adjoint solutions corresponding to aerodynamic lift and drag. The idea of the method is based upon the observation that, with appropriate boundary conditions for the linearized and adjoint problems, the adjoint variables at a particular point correspond to the functional of interest (typically, though not exclusively, aerodynamic lift or drag) evaluated using the Green's function for that point (Giles & Pierce 2000). In the analysis in Giles & Pierce (1997, 2001) for the quasi-1-D and 2-D Euler equations, the approach in each case was to construct d linearly independent source vectors $f^{(j)}(\boldsymbol{x}_0)$, which produced Green's functions $\delta U^{(j)}(\boldsymbol{x}, \boldsymbol{x}_0)$ of a simple form as solutions to the equations

$$L\delta U^{(j)}(\boldsymbol{x}, \boldsymbol{x}_0) = f^{(j)}(\boldsymbol{x}_0)\delta(\boldsymbol{x} - \boldsymbol{x}_0), \quad j = 1, \ldots, d, \tag{1.1}$$

† Email address for correspondence: lozanorc@inta.es

© The Author(s), 2022. Published by Cambridge University Press

https://doi.org/10.1017/jfm.2022.415 Published online by Cambridge University Press

where L are the linearized flow equations, $\delta(\boldsymbol{x}-\boldsymbol{x}_0)$ is the Dirac delta function and d is the number of flow equations, which is 3 for quasi-1-D flow and 4 for 2-D compressible inviscid flow. If $I^{(j)}(\boldsymbol{x}_0)$ is the value of the linear functional evaluated with $\delta U^{(j)}(\boldsymbol{x},\boldsymbol{x}_0)$ and ψ is the adjoint state associated with that functional then, by definition, and provided that suitable boundary conditions hold,

$$I^{(j)}(\boldsymbol{x}_0)=\psi^T f^{(j)}(\boldsymbol{x}_0), \tag{1.2}$$

and hence the adjoint variables can be computed from $I^{(j)}(\boldsymbol{x}_0)$ by inverting (1.2).

The above program provides insight into the nature of the Green's function and the adjoint solution, making it possible in particular to locate singularities and discontinuities in the adjoint variables. Furthermore, given a numerical adjoint solution and a set of source vectors $f^{(j)}$, the corresponding linear functionals $I^{(j)}$ can be evaluated using (1.2), providing a means of verifying several adjoint solution properties.

The adjoint equations were introduced for design optimization in the field of computational aerodynamics by Jameson (1988), and have been since extended to a variety of applications such as error estimation and mesh adaptation (Venditti & Darmofal 2002) and stability analysis (Luchini & Bottaro 2014), among many others. From the computational viewpoint, adjoint methods can be devised in two ways (Nadarajah & Jameson 2000), which differ in how the discretized adjoint equations are obtained. In the continuous approach, one discretizes the adjoint partial differential equation, while in the discrete approach, the adjoint equations are obtained directly from the discretized flow equations. An important step in the application of adjoint methods is the development and verification of adjoint codes. This task is complicated by the lack of benchmark test cases, including exact solutions, and verification is usually done indirectly by comparing sensitivities with finite differences, which may lead to erroneous conclusions (Lozano & Ponsin 2012), or (in the case of discrete adjoint solvers) by cross-checking with the linearized solver (Giles *et al.* 2003).

From a very early stage, and starting with Jameson's groundbreaking work, developments in adjoint methods have traditionally focused on the application of the method to the optimal design (Peter & Dwight 2010) of aircrafts (Kenway *et al.* 2019), ships (Kroger, Kuhl & Rung 2018) and automobiles (Othmer 2014), or to goal-oriented mesh adaptation (Fidkowski & Darmofal 2011). Comparatively less effort has been put on analysing the properties of the adjoint solutions, with some notable exceptions starting with the work of Giles & Pierce (1997, 1998, 2001) (see also Baeza *et al.* 2009; Marta *et al.* 2013; Lozano 2018, 2019*b*; Peter, Renac & Labbé 2022). A few exact solutions to the adjoint equations are known. For quasi-1-D inviscid flows, the Green's function approach has provided a tool to generate exact adjoint solutions (Giles & Pierce 2001; Lozano 2018) in terms of the base flow solution. In inviscid 2-D/3-D flows, the entropy variables provide another exact solution for an output measuring net entropy flux across boundaries (Fidkowski & Roe 2010; Lozano 2019*a*). A closely related solution, corresponding to a nearfield computation of aerodynamic drag, has been recently discovered by the authors (Lozano & Ponsin 2021*a*). Finally, an exact solution for the adjoint Navier–Stokes equations corresponding to a Blasius laminar boundary layer has been derived by Kühl, Müller & Rung (2021).

In this paper, we present a closed-form adjoint solution for the two-dimensional incompressible Euler equations for irrotational base flows based on the Green's function approach. This solution provides a cheap adjoint field for design or adaptation purposes that, perhaps more importantly in practical terms, can also serve for verification and debugging of adjoint solvers. However, they can also serve to disentangle the properties

https://doi.org/10.1017/jfm.2022.415 Published online by Cambridge University Press

of the solutions to the adjoint equations, which, despite being linear partial differential equations, give rise to a rich zoo of structures comprising singularities along stagnation streamlines, stagnation points and sharp trailing edges (Giles & Pierce 1997, 1999, 2002; Lozano 2019*b*), and also to confirm the existence of an adjoint singularity at solid walls suggested by recent results (Peter *et al.* 2022) that could explain the numerical divergence first observed by Lozano (2019*b*).

2. 2-D incompressible adjoint Euler equations

To be as self-contained as possible, and to fix notation, we begin by recalling a few facts regarding the adjoint equations. In the present paper, we will concentrate on the incompressible Euler equations and consider linearizations around an irrotational base flow. It is well known that in such a case, the base flow can be derived either from a potential or a stream function that obey Laplace's equation. We could consider perturbations to this Laplace equation which would lead to an adjoint solution obeying the Laplace equation as well (as in e.g. Giles & Pierce 1999). We will not follow this approach here. Instead, we will consider perturbations to the full incompressible Euler equations and obtain the corresponding full incompressible adjoint Euler equations, and specialize later to perturbations around an irrotational base flow.

We will focus, for definiteness, on a steady, two-dimensional, incompressible, inviscid flow on a domain Ω with far-field boundary S^∞ and wall boundary S (typically an airfoil profile). The flow is governed by the incompressible Euler equations:

$$R(U) = \nabla \cdot \boldsymbol{F}(U) = 0, \tag{2.1}$$

where

$$U = \begin{pmatrix} p \\ \rho u \\ \rho v \end{pmatrix}, \quad \boldsymbol{F} = \begin{pmatrix} \rho \boldsymbol{v} \\ \rho \boldsymbol{v} u + p\hat{x} \\ \rho \boldsymbol{v} v + p\hat{y} \end{pmatrix}. \tag{2.2a,b}$$

Here, ρ is the (constant) density, $\boldsymbol{v} = (u, v) = (q\cos\phi, q\sin\phi)$ is the velocity (where $q^2 = u^2 + v^2$ and ϕ is the local flow angle), p is the pressure and $\hat{x}$, $\hat{y}$ are the Cartesian unit vectors. The flow obeys a non-transpiration boundary condition $\boldsymbol{v} \cdot \hat{n} = 0$ on S (where $\hat{n}$ is the outward-pointing unit normal vector at the boundary) and it is assumed to approach the far-field state $(q_\infty \cos\alpha, q_\infty \sin\alpha)$ at the far-field S^∞, α being the angle of attack.

To set-up the adjoint problem, an objective function needs to be defined, which is taken to be the lift or drag coefficient

$$I = \int_S C_p (\hat{n} \cdot \boldsymbol{d})\, \mathrm{d}s, \tag{2.3}$$

where $\boldsymbol{d} = \boldsymbol{d}_D = (\cos\alpha, \sin\alpha)$ for drag and $\boldsymbol{d} = \boldsymbol{d}_L = (-\sin\alpha, \cos\alpha)$ for lift, $C_p = c_\infty^{-1}(p - p_\infty)$ is the non-dimensional pressure coefficient, p_∞ is the pressure of the free stream state at the far-field and $c_\infty = \rho_\infty q_\infty^2 \ell/2$ is a normalization factor (ℓ is a reference length). We also need to consider linear perturbations to (2.1) and (2.3). For definiteness, we will focus on design applications, for which perturbations in the flow solution, $\delta U = (\delta p, \rho\delta u, \rho\delta v)^T$, arise as a result of changes, $\delta \boldsymbol{x}$, in the geometry of the

https://doi.org/10.1017/jfm.2022.415 Published online by Cambridge University Press

boundary S. Linearizing (2.1) with respect to δU yields

$$\nabla \cdot (\boldsymbol{A}\delta U) = f, \tag{2.4}$$

where

$$\boldsymbol{A} = \frac{\partial}{\partial(p, \rho u, \rho v)} \begin{pmatrix} \rho \boldsymbol{v} \\ \rho u \boldsymbol{v} + p\hat{x} \\ \rho v \boldsymbol{v} + p\hat{y} \end{pmatrix} = \begin{pmatrix} 0 & \hat{x} & \hat{y} \\ \hat{x}\boldsymbol{v} + u\hat{x} & u\hat{y} \\ \hat{y} & v\hat{x} & \boldsymbol{v} + v\hat{y} \end{pmatrix}, \tag{2.5}$$

are the flux Jacobians and the residual f is typically zero for shape optimization problems. Here, δU obeys the following boundary condition at solid walls:

$$\delta \boldsymbol{v} \cdot \hat{n} = w \text{ on } S, \tag{2.6}$$

where $w = -\boldsymbol{v} \cdot \delta\hat{n} - [(\delta \boldsymbol{x} \cdot \nabla)\boldsymbol{v}] \cdot \hat{n}$, with $\delta\hat{n}$ being the variation in the boundary normal induced by the deformation of the geometry. In the far-field, δU is chosen such that there is no perturbation to the flow far-field boundary conditions, unless one is specifically considering the effect of perturbations in far-field parameters such as angle of attack.

The variation of the cost function (2.3) with respect to perturbations in the flow and the geometry is (Anderson & Venkatakrishnan 1999; Castro *et al.* 2007; Delfour & Zolésio 2011)

$$\delta I = \int_S c_\infty^{-1} (\boldsymbol{d} \cdot \hat{n}) \delta p \, \mathrm{d}s + \int_S c_\infty^{-1} (\delta \boldsymbol{x} \cdot \hat{n})(\boldsymbol{d} \cdot \nabla p) \, \mathrm{d}s, \tag{2.7}$$

where δp reflects the variation of the solution in response to the changing geometry.

Equation (2.7) can be efficiently computed with the adjoint approach (Jameson 1988), where adjoint variables $\psi = (\psi_1, \boldsymbol{\varphi})^T$, with $\boldsymbol{\varphi} = (\psi_2, \psi_3)$, are introduced over the entire flow domain, and the objective function I is reformulated as

$$L = I - \int_\Omega \psi^T R(U) \, \mathrm{d}\Omega. \tag{2.8}$$

Linearizing the Lagrangian (2.8) with respect to flow and geometry perturbations gives

$$\begin{aligned} \delta L = &\int_S c_\infty^{-1} (\boldsymbol{d} \cdot \hat{n}) \delta p \, \mathrm{d}s + \int_S c_\infty^{-1} (\delta \boldsymbol{x} \cdot \hat{n})(\boldsymbol{d} \cdot \nabla p) \, \mathrm{d}s \\ &- \int_\Omega \psi^T \nabla \cdot (\boldsymbol{A}\delta U) \, \mathrm{d}\Omega + \int_\Omega \psi^T f \, \mathrm{d}\Omega. \end{aligned} \tag{2.9}$$

After integration by parts and rearrangement, this yields (Anderson & Venkatakrishnan 1999; Castro *et al.* 2007):

$$\begin{aligned} \delta L = &\int_S c_\infty^{-1} (\boldsymbol{d} \cdot \hat{n}) \delta p \, \mathrm{d}s + \int_S c_\infty^{-1} (\delta \boldsymbol{x} \cdot \hat{n})(\boldsymbol{d} \cdot \nabla p) \, \mathrm{d}s + \int_\Omega \nabla \psi^T \cdot \boldsymbol{A}\delta U \, \mathrm{d}\Omega \\ &- \int_S \psi^T \hat{n} \cdot \boldsymbol{A}\delta U \, \mathrm{d}s - \int_{S_\infty} \psi^T \hat{n} \cdot \boldsymbol{A}\delta U \, \mathrm{d}s + \int_\Omega \psi^T f \, \mathrm{d}\Omega \\ = &\int_\Omega \nabla \psi^T \cdot \boldsymbol{A}\delta U \, \mathrm{d}\Omega + \int_S (c_\infty^{-1} (\boldsymbol{d} \cdot \hat{n}) - \hat{n} \cdot \boldsymbol{\varphi}) \delta p \, \mathrm{d}s - \int_{S_\infty} \psi^T \hat{n} \cdot \boldsymbol{A}\delta U \, \mathrm{d}s \\ &+ \int_S c_\infty^{-1} (\delta \boldsymbol{x} \cdot \hat{n})(\boldsymbol{d} \cdot \nabla p) \, \mathrm{d}s + \int_\Omega \psi^T f \, \mathrm{d}\Omega - \int_S \rho \hat{n} \cdot \delta \boldsymbol{v} (\psi_1 + \boldsymbol{v} \cdot \boldsymbol{\varphi}) \, \mathrm{d}s. \end{aligned} \tag{2.10}$$

https://doi.org/10.1017/jfm.2022.415 Published online by Cambridge University Press

From (2.10), it follows that if the adjoint state obeys the following adjoint equations and boundary conditions:

$$\left.\begin{aligned} &\boldsymbol{A}^T \cdot \nabla \psi = 0 \qquad \text{in } \Omega \\ &\hat{n} \cdot \boldsymbol{\varphi} = c_\infty^{-1} (\boldsymbol{d} \cdot \hat{n}) \text{at } S \\ &\psi^T \hat{n} \cdot \boldsymbol{A} \delta U = 0 \quad \text{at } S_\infty \end{aligned}\right\}, \tag{2.11}$$

then the last two lines in (2.10) yield the (continuous) adjoint-based sensitivity derivatives

$$\delta \int_S C_p (\hat{n} \cdot \boldsymbol{d}) \, \mathrm{d}s = \int_\Omega \psi^T f \, \mathrm{d}\Omega + \int_S {c_\infty}^{-1} (\delta \boldsymbol{x} \cdot \hat{n})(\boldsymbol{d} \cdot \nabla p) \, \mathrm{d}s - \int_S w \rho (\psi_1 + \boldsymbol{v} \cdot \boldsymbol{\varphi}) \, \mathrm{d}s. \tag{2.12}$$

Equation (2.12) lacks the Leibniz term $\int_S (\delta \boldsymbol{x} \cdot \hat{n}) \, \psi^T \nabla \cdot \boldsymbol{F} \, \mathrm{d}s$, first introduced in Kavvadias, Papoutsis-Kiachagias & Giannakoglou (2015) (see also Lozano 2017), which is zero analytically. Finally, when far-field parameters (such as angle of attack) are considered as design variables, the contribution from the far-field integral $\int_{S_\infty} \psi^T \hat{n} \cdot \boldsymbol{A} \delta U \, \mathrm{d}s$ should also be included in (2.12).

3. Using Green's functions to compute the analytic adjoint solution

The Green's function approach was completed with a closed-form solution for the adjoint quasi-1-D Euler equations in Giles & Pierce (2001) and outlined for the 2-D Euler equations in Giles & Pierce (1997), where four linearly independent source vectors representing mass, normal force, enthalpy and stagnation pressure perturbations were considered. The first two reduce, for incompressible flow, to point mass sources and point vortices, respectively, which are well-known elementary solutions in potential flow; the third one yields zero lift or drag perturbation, and the final one was shown to lead to a non-uniform mass perturbation along the streamline downstream of the insertion point that would be responsible for an adjoint singularity along the incoming stagnation streamline.

Focusing now on 2-D incompressible flow, suppose that we have three point perturbations $\delta U^{(j)}(\boldsymbol{x}, \boldsymbol{x}_0), j = 1, \ldots, 3$, that obey the linearized equations

$$\nabla \cdot (\boldsymbol{A} \delta U^{(j)}(\boldsymbol{x}, \boldsymbol{x}_0)) = f^{(j)}(\boldsymbol{x}_0) \delta (\boldsymbol{x} - \boldsymbol{x}_0), \tag{3.1}$$

with the following wall boundary conditions:

$$\delta \boldsymbol{v}^{(j)}(\boldsymbol{x}, \boldsymbol{x}_0) \cdot \hat{n} = 0, \quad \boldsymbol{x} \in S, \tag{3.2}$$

and far-field boundary conditions such that there is no perturbation to the inflow state. In (3.1), $\boldsymbol{x}$ is a generic point in the fluid domain, $\boldsymbol{x}_0$ is the location of the singularity and the gradient operator on the left-hand side of the equation acts on $\boldsymbol{x}$. If

$$I^{(j)}(\boldsymbol{x}_0) = c_\infty^{-1} \int_S \boldsymbol{d} \cdot \hat{n} \partial_U p \delta U^{(j)}(\boldsymbol{x}, \boldsymbol{x}_0) \, \mathrm{d}s \tag{3.3}$$

is the value of the linearized functional (lift or drag) corresponding to $\delta U^{(j)}(\boldsymbol{x}, \boldsymbol{x}_0)$, then we can apply (2.10)–(2.12) to $\delta U^{(j)}(\boldsymbol{x}, \boldsymbol{x}_0)$ and we get

$$I^{(j)}(\boldsymbol{x}_0) = \psi^T(\boldsymbol{x}_0) f^{(j)}(\boldsymbol{x}_0). \tag{3.4}$$

If the source vectors $f^{(j)}(\boldsymbol{x}_0)$ are linearly independent, (3.4) can be inverted to obtain the adjoint variables in terms of the linearized cost functions

$$\psi^T(\boldsymbol{x}_0) = (I^{(1)}, I^{(2)}, I^{(3)}) \cdot (f^{(1)} | f^{(2)} | f^{(3)})^{-1}, \tag{3.5}$$

where $(f^{(1)} | f^{(2)} | f^{(3)})$ is a matrix whose columns are the vectors $f^{(j)}$.

https://doi.org/10.1017/jfm.2022.415 Published online by Cambridge University Press

Following Giles & Pierce (1997), we now define three linearly independent perturbations, which we take to be a point source, a point vortex and a stagnation pressure perturbation at fixed pressure and local flow angle.

3.1. *Point source*

The first perturbation is a point mass source located at $\boldsymbol{x}_0$. In unbounded space, the response to this perturbation is given by the free-space solution:

$$\delta U^{(1)}_{free} = \begin{pmatrix} \delta p^{(1)}_{free} \\ \rho\delta u^{(1)}_{free} \\ \rho\delta v^{(1)}_{free} \end{pmatrix} = \frac{\varepsilon}{2\pi} \begin{pmatrix} -(u\partial_x + v\partial_y)(\ln r) \\ \partial_x \ln r \\ \partial_y \ln r \end{pmatrix}, \tag{3.6}$$

($r = |\boldsymbol{x} - \boldsymbol{x}_0|$ and ε is an arbitrary constant point singularity strength that we introduce for convenience and that we will set to 1 in the end), which obeys the following linearized equations:

$$\begin{aligned} \boldsymbol{\nabla}\cdot(\boldsymbol{A}\delta U^{(1)}_{free}) &= \begin{pmatrix} \rho\boldsymbol{\nabla}\cdot\delta\boldsymbol{v}^{(1)}_{free} \\ \rho\boldsymbol{v}\cdot\boldsymbol{\nabla}\delta u^{(1)}_{free} + \rho u\boldsymbol{\nabla}\cdot\delta\boldsymbol{v}^{(1)}_{free} + \rho\delta\boldsymbol{v}^{(1)}_{free}\cdot\boldsymbol{\nabla}u + \partial_x\delta p^{(1)}_{free} \\ \rho\boldsymbol{v}\cdot\boldsymbol{\nabla}\delta v^{(1)}_{free} + \rho v\boldsymbol{\nabla}\cdot\delta\boldsymbol{v}^{(1)}_{free} + \rho\delta\boldsymbol{v}^{(1)}_{free}\cdot\boldsymbol{\nabla}v + \partial_y\delta p^{(1)}_{free} \end{pmatrix} \\ &= \varepsilon \begin{pmatrix} 1 \\ u \\ v \end{pmatrix} \delta(\boldsymbol{x} - \boldsymbol{x}_0) + \tfrac{\varepsilon}{2\pi} \begin{pmatrix} 0 \\ (\partial_y u - \partial_x v)\partial_y \ln r \\ -(\partial_y u - \partial_x v)\partial_x \ln r \end{pmatrix}, \end{aligned} \tag{3.7}$$

where the second term on the right-hand side vanishes if the base flow is irrotational. Hence, the source vector is

$$f^{(1)} = \varepsilon \begin{pmatrix} 1 \\ u \\ v \end{pmatrix}. \tag{3.8}$$

Notice that $\psi^T f^{(1)} = \varepsilon(\psi_1 + \boldsymbol{v}\cdot\boldsymbol{\varphi})$, so $I^{(1)}$ is related to the (continuous) adjoint-based lift/drag gradient (2.12).

The Green's function approach requires the value of the linearized functionals $I^{(1)}$, which are the lift and drag forces exerted by the point source on a body. In the presence of a body, the above functional form (3.6) only holds locally near the singularity, such that (3.8) still holds, but needs to be modified globally to account for the wall boundary condition. This is particularly simple in 2-D potential flow using a complex variable and the method of images, and allows us to compute the force on immersed bodies using Blasius theorem (Milne-Thomson 1962). The simplest problem where the body is a circle is a standard academic exercise, and more general situations can be derived from this with suitable conformal transformations. The complex force on the cylinder turns out to be $w_I - q_\infty \mathrm{e}^{-\mathrm{i}\alpha}$, where w_I is the induced velocity at the point singularity and $q_\infty \mathrm{e}^{-\mathrm{i}\alpha}$ is the free stream complex velocity (here $q_\infty = \sqrt{u_\infty^2 + v_\infty^2}$). An interesting fact is that the same expression yields the force on a body of arbitrary shape (Milne-Thomson 1962), a result that is known as Lagally's theorem. Hence, the force exerted by the point source on the

https://doi.org/10.1017/jfm.2022.415 Published online by Cambridge University Press

body is, keeping only terms linear in the source strength ε,

$$\delta D^{(1)} - i\delta L^{(1)} = \varepsilon\, \mathrm{e}^{\mathrm{i}\alpha}(u - iv - q_\infty\, \mathrm{e}^{-\mathrm{i}\alpha}) + O(\varepsilon^2). \tag{3.9}$$

Here, $\delta D^{(1)}$ and $\delta L^{(1)}$ stand for the linear perturbations to drag and lift, respectively, due to the point source. Equation (3.9) thus gives the linearized force exerted by a point source on a rigid body of arbitrary shape in terms of the undisturbed velocity at the source, $u - iv$. This is not the end of the story though. Potential flows contain circulation, which can be freely adjusted *a priori*. For bodies with sharp trailing edges, the value of the circulation is fixed by the Kutta condition that asserts that the flow contains the precise amount of circulation to make the flow smooth at the trailing edge. The introduction of a point source disturbs the flow at the trailing edge, so the circulation has to be adjusted accordingly to preserve the smooth flow at the trailing edge. The extra circulation contributes an additional term to (3.9) that we shall calculate shortly. For blunt bodies, however, the circulation is not fixed by any smoothness requirement. However, it turns out that to obtain consistent adjoint solutions, a Kutta condition has to be imposed as well, ensuring no perturbation to the position of the rear stagnation point (see § 3.2.1).

To obtain explicit formulae, we will consider an airfoil in the complex z plane with a sharp trailing edge at $z = 1$. Let us suppose that the airfoil is transformed into a circle of radius R and centred at ζ_0 in the auxiliary complex ζ-plane by a conformal mapping $z = F(\zeta)$ (with $F(\zeta) \to 1$ as $|\zeta| \to \infty$), such that the point ζ_{te} on the circle is transformed into the trailing edge of the airfoil at $z = 1$. The (irrotational) base flow around the circle can be derived from the complex potential:

$$\Phi(\zeta) = q_\infty\, \mathrm{e}^{-\mathrm{i}\alpha}(\zeta - \zeta_0) + q_\infty\, \mathrm{e}^{\mathrm{i}\alpha}\frac{R^2}{\zeta - \zeta_0} - \frac{i\Gamma_0}{2\pi}\ln(\zeta - \zeta_0). \tag{3.10}$$

The corresponding potential at a point z on the airfoil plane is precisely $\Phi(\zeta(z))$. In the unperturbed flow, the circulation Γ_0 around the circle has to be fixed to the value

$$\Gamma_0 = -2\pi i q_\infty\, \mathrm{e}^{-\mathrm{i}\alpha}(\zeta_{te} - \zeta_0) + 2\pi i q_\infty\, \mathrm{e}^{\mathrm{i}\alpha}\frac{R^2}{\zeta_{te} - \zeta_0}, \tag{3.11}$$

such that the flow around the circle has a stagnation point at ζ_{te}, i.e.

$$W(\zeta_{te}) = \mathrm{d}\Phi/\mathrm{d}\zeta|_{\zeta=\zeta_{te}} = q_\infty\, \mathrm{e}^{-\mathrm{i}\alpha} - q_\infty\, \mathrm{e}^{\mathrm{i}\alpha}\frac{R^2}{(\zeta_{te} - \zeta_0)^2} - \frac{i\Gamma_0}{2\pi}\frac{1}{\zeta_{te} - \zeta_0} = 0. \tag{3.12}$$

After inserting a point source at ζ_s, the potential picks an extra contribution from the point source and its images with respect to the circle (Milne-Thomson 1962):

$$\Phi_s(\zeta) = \frac{\varepsilon}{2\pi\rho}\ln(\zeta - \zeta_s) + \frac{\varepsilon}{2\pi\rho}\ln\left(\zeta - \zeta_0 - \frac{R^2}{\overline{\zeta_s} - \overline{\zeta_0}}\right) - \frac{\varepsilon}{2\pi\rho}\ln(\zeta - \zeta_0), \tag{3.13}$$

where $\bar{\zeta}$ denotes the complex conjugate of ζ. Here, $\Phi_s(\zeta)$ induces a non-zero velocity at ζ_{te},

$$W_s(\zeta_{te}) = \frac{\varepsilon}{2\pi\rho(\zeta_{te} - \zeta_s)} + \frac{\varepsilon}{2\pi\rho}\frac{1}{\zeta_{te} - \zeta_0 - \frac{R^2}{\overline{\zeta_s} - \overline{\zeta_0}}} - \frac{\varepsilon}{2\pi\rho(\zeta_{te} - \zeta_0)}, \tag{3.14}$$

which has to be cancelled with additional circulation

$$\delta\Gamma_0 = -2\pi i(\zeta_{te} - \zeta_0)W_s(\zeta_{te}). \tag{3.15}$$

https://doi.org/10.1017/jfm.2022.415 Published online by Cambridge University Press

This extra circulation produces an extra force that has to be added to (3.9):

$$\begin{aligned}\delta D^{(1)} - i\delta L^{(1)} &= i\rho q_\infty \delta\Gamma_0 + \varepsilon\, \mathrm{e}^{\mathrm{i}\alpha}(u - iv - q_\infty\, \mathrm{e}^{-\mathrm{i}\alpha}) + O(\varepsilon^2)\\ &= 2\pi\rho q_\infty(\zeta_{te} - \zeta_0)W_s(\zeta_{te}) + \varepsilon\, \mathrm{e}^{\mathrm{i}\alpha}(u - iv - q_\infty\, \mathrm{e}^{-\mathrm{i}\alpha}) + O(\varepsilon^2)\\ &= -\varepsilon q_\infty \left(\frac{\zeta_{te} - \zeta_0}{\zeta_s - \zeta_{te}} - \frac{\overline{\zeta_{te}} - \overline{\zeta_0}}{\overline{\zeta_s} - \overline{\zeta_{te}}}\right) + \varepsilon\, \mathrm{e}^{\mathrm{i}\alpha}(u - iv - q_\infty\, \mathrm{e}^{-\mathrm{i}\alpha}) + O(\varepsilon^2). \end{aligned} \tag{3.16}$$

Notice that the extra term is purely imaginary, so it only affects lift. Separating the real and imaginary parts, setting $\varepsilon = 1$ and dividing by c_∞ to normalize, we get the following linearized functionals due to the point source:

$$\left.\begin{aligned} I_D^{(1)}(z(\zeta)) &= \tfrac{1}{c_\infty}(u(z(\zeta))\cos\alpha + v(z(\zeta))\sin\alpha - q_\infty),\\ I_L^{(1)}(z(\zeta)) &= \tfrac{1}{c_\infty}(v(z(\zeta))\cos\alpha - u(z(\zeta))\sin\alpha) - i\tfrac{q_\infty}{c_\infty}\left(\frac{\zeta_{te} - \zeta_0}{\zeta(z) - \zeta_{te}} - \frac{\overline{\zeta_{te}} - \overline{\zeta_0}}{\overline{\zeta}(z) - \overline{\zeta_{te}}}\right). \end{aligned}\right\} \tag{3.17}$$

Notice that the extra contribution is independent of the initial circulation and blows up at the trailing edge, thus providing a precise mechanism (and an explanation) for the adjoint singularity at the trailing edge.

3.2. *Point vortex*

The second perturbation is a point vortex. In unbounded space it is simply

$$\delta U^{(2)}_{free} = \begin{pmatrix} \delta p^{(2)}_{free} \\ \rho\delta u^{(2)}_{free} \\ \rho\delta v^{(2)}_{free} \end{pmatrix} = \frac{\varepsilon}{2\pi}\begin{pmatrix} (v\partial_x - u\partial_y)(\ln r) \\ \partial_y \ln r \\ -\partial_x \ln r \end{pmatrix}. \tag{3.18}$$

This solution obeys the linearized equation

$$\begin{aligned} \boldsymbol{\nabla}\cdot(\boldsymbol{A}\delta U^{(2)}_{free}) &= \begin{pmatrix} \rho\boldsymbol{\nabla}\cdot\delta\boldsymbol{v}^{(2)}_{free} \\ \rho\boldsymbol{v}\cdot\boldsymbol{\nabla}\delta u^{(2)}_{free} + \rho u\boldsymbol{\nabla}\cdot\delta\boldsymbol{v}^{(2)}_{free} + \rho\delta\boldsymbol{v}^{(2)}_{free}\cdot\boldsymbol{\nabla}u + \partial_x\delta p^{(2)}_{free} \\ \rho\boldsymbol{v}\cdot\boldsymbol{\nabla}\delta v^{(2)}_{free} + \rho v\boldsymbol{\nabla}\cdot\delta\boldsymbol{v}^{(2)}_{free} + \rho\delta\boldsymbol{v}^{(2)}_{free}\cdot\boldsymbol{\nabla}v + \partial_y\delta p^{(2)}_{free} \end{pmatrix} \\ &= \varepsilon\begin{pmatrix} 0 \\ v \\ -u \end{pmatrix}\delta(\boldsymbol{x} - \boldsymbol{x}_0) + \tfrac{\varepsilon}{2\pi}\begin{pmatrix} 0 \\ (\partial_x v - \partial_y u)\partial_x \ln r \\ (\partial_x v - \partial_y u)\partial_y \ln r \end{pmatrix}, \end{aligned} \tag{3.19}$$

where the extra term vanishes if the base flow is irrotational. Hence, the source vector is

$$f^{(2)} = \varepsilon\begin{pmatrix} 0 \\ v \\ -u \end{pmatrix}. \tag{3.20}$$

Notice that $\psi^T f^{(2)} = \varepsilon(v\psi_2 - u\psi_3)$, so $I^{(2)}$ approaches $q\hat{n}_S\cdot\boldsymbol{\varphi}$ as the vortex approaches the wall. Its value is thus constrained by the adjoint wall boundary condition $\hat{n}_S\cdot\boldsymbol{\varphi} = c_\infty^{-1}(\boldsymbol{d}\cdot\hat{n}_S)$ (Giles & Pierce 1997).

https://doi.org/10.1017/jfm.2022.415 Published online by Cambridge University Press

Once again, in the presence of a body, the above functional form needs to be modified to account for the wall boundary condition. The correct expression can then be used to compute the force exerted by the vortex on a body, which poses no significant difficulties relative to the source case, so we just quote the results. The linearized complex force, taking into account the Kutta condition, is

$$\begin{aligned}\delta D^{(2)} - i\delta L^{(2)} &= 2\pi\rho q_\infty(\zeta_{te}-\zeta_0)W_v(\zeta_{te}) + i\varepsilon\,\mathrm{e}^{\mathrm{i}\alpha}(u - iv - q_\infty\,\mathrm{e}^{-\mathrm{i}\alpha}) + O(\varepsilon^2)\\ &= -i\varepsilon q_\infty\left(\frac{\zeta_{te}-\zeta_0}{\zeta_s-\zeta_{te}} + \frac{\overline{\zeta_{te}}-\overline{\zeta_0}}{\overline{\zeta_s}-\overline{\zeta_{te}}}\right) + i\varepsilon\,\mathrm{e}^{\mathrm{i}\alpha}(u - iv - q_\infty\,\mathrm{e}^{-\mathrm{i}\alpha}) + O(\varepsilon^2),\end{aligned} \tag{3.21}$$

where $W_v(\zeta_{te})$ is the complex velocity induced by the vortex (and its images) at ζ_{te}. Hence, the properly normalized linearized functionals due to the vortex are (setting $\varepsilon = 1$)

$$\left.\begin{aligned} I_D^{(2)}(\zeta) &= \tfrac{1}{c_\infty}(v(z(\zeta))\cos\alpha - u(z(\zeta))\sin\alpha)\\ I_L^{(2)}(z(\zeta)) &= -\tfrac{1}{c_\infty}(u(z(\zeta))\cos\alpha + v(z(\zeta))\sin\alpha - q_\infty) + \tfrac{q_\infty}{c_\infty}\left(\frac{\zeta_{te}-\zeta_0}{\zeta_s-\zeta_{te}} + \frac{\overline{\zeta_{te}}-\overline{\zeta_0}}{\overline{\zeta_s}-\overline{\zeta_{te}}}\right)\end{aligned}\right\}. \tag{3.22}$$

Notice that the extra term diverges as the vortex approaches the trailing edge. Notice that along the wall, we have $|\zeta_s - \zeta_0| = R$ and, thus,

$$\frac{\zeta_{te}-\zeta_0}{\zeta_s-\zeta_{te}} + \frac{\overline{\zeta_{te}}-\overline{\zeta_0}}{\overline{\zeta_s}-\overline{\zeta_{te}}} = -1, \tag{3.23}$$

so that

$$I_L^{(2)}|_{wall} = -\tfrac{1}{c_\infty}(u\cos\alpha + v\sin\alpha), \tag{3.24}$$

as required by the adjoint wall boundary condition.

3.2.1. *Blunt bodies*

For blunt bodies (circle, ellipse), there is no need to impose a Kutta condition, so the circulation is *a priori* arbitrary and the above extra terms disappear. However, the resulting forces are not consistent with the adjoint approach (as we have discussed above, the force exerted by a point vortex has to approach the wall in a certain fashion so that the adjoint wall boundary condition is obeyed) and the Green's function approach leads to the wrong lift-based adjoint solution. It turns out that to obtain a sensible solution, it is necessary to assume that an adjoint-consistent linearization requires a Kutta condition such that the rear stagnation point is not disturbed by the point singularities. This requirement results in the extra forces described above, and the linearized functionals are precisely (3.17) and (3.22) and lead to an analytic adjoint solution that obeys the adjoint equations and boundary conditions and that agrees with numerical computations (see, for example, the adjoint solution for a 6:1 ellipse presented in Lozano & Ponsin 2021*b*).

3.3. *Change in stagnation pressure at fixed p*

For the final perturbation we choose, in analogy with Giles & Pierce (1997), a perturbation to the stagnation pressure $p_0 = p + \frac{1}{2}\rho q^2$ (where $q^2 = u^2 + v^2$) at fixed values of the pressure and the local flow angle ϕ. As stagnation pressure is convected along streamlines,

https://doi.org/10.1017/jfm.2022.415 Published online by Cambridge University Press

we expect the solution to be concentrated along the streamline downstream of the insertion point $\boldsymbol{x}_0$. Following Giles & Pierce (1997), we use curvilinear streamline coordinates in which s is the distance along the streamline downstream of the insertion point and n is the coordinate perpendicular to the streamline. In these coordinates, the perturbation is, in a first approximation,

$$\varepsilon H(s)\delta(n)\frac{1}{q}\left(\frac{\partial U}{\partial p_0}\right)_{p,\phi}(\boldsymbol{x}) = \frac{\varepsilon}{q^3}\begin{pmatrix}0\\ u\\ v\end{pmatrix}(\boldsymbol{x})H(s)\delta(n), \tag{3.25}$$

where $H(s)$ is the Heaviside step function and $\delta(n)$ is the Dirac delta function. However, as explained in Giles & Pierce (1997), this is not the full form of the solution. This fact can be understood most simply by noting that (3.25) does not obey the linearized flow equations. In fact,

$$\boldsymbol{\nabla}\cdot\left[\frac{\varepsilon}{q}\boldsymbol{A}\left(\frac{\partial U}{\partial p_0}\right)_{p,\phi}H(s)\delta(n)\right] = \boldsymbol{\nabla}\cdot[\hat{s}f^{(3)}H(s)\delta(n)], \tag{3.26}$$

where $\hat{s}$ is the unit vector in the flow direction and

$$f^{(3)} = \frac{\varepsilon}{q}\left(\frac{\partial \boldsymbol{F}\cdot\hat{s}}{\partial p_0}\right)_{p,\phi} = \frac{\varepsilon}{q^2}\begin{pmatrix}1\\ 2u\\ 2v\end{pmatrix}. \tag{3.27}$$

To proceed further, we need to express $\boldsymbol{\nabla}$ in streamline coordinates. While for smooth functions $\boldsymbol{\nabla}\cdot[\hat{s}w] = \partial_s w + w\partial_n\phi$, when delta functions are present, one needs to proceed more carefully. To this end, we follow Emanuel (2000) and define coordinates ξ_1 along the streamline and ξ_2 that parameterizes the lines orthogonal to ξ_1. The ξ_i coordinates are related to the streamline coordinates as $\mathrm{d}s = h_1\,\mathrm{d}\xi_1$ and $\mathrm{d}n = h_2\,\mathrm{d}\xi_2$, where $h_i = ||\partial\boldsymbol{x}/\partial\xi_i||$ are the scale factors. In terms of (ξ_1, ξ_2), the divergence operator acting on a vector $\boldsymbol{w}$ is

$$\boldsymbol{\nabla}\cdot\boldsymbol{w} = \frac{1}{h_1h_2}\frac{\partial}{\partial\xi_1}(h_2\boldsymbol{w}\cdot\hat{e}_1) + \frac{1}{h_1h_2}\frac{\partial}{\partial\xi_2}(h_1\boldsymbol{w}\cdot\hat{e}_2), \tag{3.28}$$

where $\hat{e}_i = h_i^{-1}\partial\boldsymbol{x}/\partial\xi_i$ are the local curvilinear unit basis vectors (note that $\hat{e}_1 \equiv \hat{s}$ in earlier notation). Finally, we need to consider the Heaviside and Dirac delta functions. Since $\iint \mathrm{d}x\,\mathrm{d}y = \iint h_1h_2\,\mathrm{d}\xi_1\,\mathrm{d}\xi_2$, we have

$$\delta(\boldsymbol{x}) \equiv \delta(x)\delta(y) = \delta(\xi_1)\delta(\xi_2)/h_1h_2, \tag{3.29}$$

and

$$H(s)\delta(n) \equiv H(\xi_1)\delta(\xi_2)/h_2. \tag{3.30}$$

Hence,

$$\begin{aligned}\boldsymbol{\nabla}\cdot(f^{(3)}\hat{s}H(s)\delta(n)) &= \frac{1}{h_1h_2}\frac{\partial}{\partial\xi_1}(H(\xi_1)\delta(\xi_2)f^{(3)})\\ &= \frac{1}{h_1h_2}\delta(\xi_1)\delta(\xi_2)f^{(3)} + \frac{H(\xi_1)\delta(\xi_2)}{h_2}\frac{1}{h_1}\frac{\partial}{\partial\xi_1}f^{(3)}\\ &= \delta(\boldsymbol{x}-\boldsymbol{x}_0)f^{(3)} + H(s)\delta(n)\frac{\partial}{\partial s}f^{(3)}.\end{aligned} \tag{3.31}$$

https://doi.org/10.1017/jfm.2022.415 Published online by Cambridge University Press

Using $(u, v) = (q\cos\phi, q\sin\phi)$, the last term on the right-hand side can be further expanded as

$$\frac{\partial}{\partial s} f^{(3)} = f^{(1)} \partial_s q^{-2} - \frac{2}{q^2} f^{(2)} \partial_s \phi, \tag{3.32}$$

where

$$f^{(1)} = \varepsilon \begin{pmatrix} 1 \\ u \\ v \end{pmatrix}, \quad f^{(2)} = \varepsilon \begin{pmatrix} 0 \\ v \\ -u \end{pmatrix}, \tag{3.33a,b}$$

are the source vectors for the point source and vortex, respectively. Hence, we can write the full solution as

$$\begin{aligned} \delta U^{(3)}(\boldsymbol{x}, \boldsymbol{x}_0) &= \varepsilon H(s)\delta(n) \frac{1}{q} \left(\frac{\partial U}{\partial p_0} \right)_{p,\phi} (\boldsymbol{x}) \\ &\quad - \iint h_1 h_2 \, \mathrm{d}\xi'_1 \, \mathrm{d}\xi'_2 \frac{H(\xi'_1 - \xi_1^0)\delta(\xi'_2 - \xi_2^0)}{h_2} \partial_s q^{-2}(\boldsymbol{x}') \delta U^{(1)}(\boldsymbol{x}, \boldsymbol{x}') \\ &\quad + \iint h_1 h_2 \, \mathrm{d}\xi'_1 \, \mathrm{d}\xi'_2 \frac{H(\xi'_1 - \xi_1^0)\delta(\xi'_2 - \xi_2^0)}{h_2} \frac{2}{q^2} \partial_s \phi(\boldsymbol{x}') \delta U^{(2)}(\boldsymbol{x}, \boldsymbol{x}') \\ &= \varepsilon H(s)\delta(n) \frac{1}{q} \left(\frac{\partial U}{\partial p_0} \right)_{p,\phi} (\boldsymbol{x}) - \int_0^\infty \mathrm{d}s' \partial_s q^{-2}(\boldsymbol{x}(s')) \delta U^{(1)}(\boldsymbol{x}, \boldsymbol{x}(s')) \\ &\quad + \int_0^\infty \mathrm{d}s' \frac{2}{q^2} \partial_s \phi(\boldsymbol{x}(s')) \delta U^{(2)}(\boldsymbol{x}, \boldsymbol{x}(s')), \end{aligned} \tag{3.34}$$

where $\delta U^{(1)}$, $\delta U^{(2)}$ are the complete point source and point vortex Green's functions (i.e. respecting the wall boundary conditions), which reduce to (3.6) and (3.18), respectively, in the vicinity of the singularity. We can check that (3.34) obeys

$$\boldsymbol{\nabla} \cdot (\boldsymbol{A} \delta U^{(3)}(\boldsymbol{x}, \boldsymbol{x}_0)) = f^{(3)}(\boldsymbol{x}) \delta(\boldsymbol{x} - \boldsymbol{x}_0) = f^{(3)}(\boldsymbol{x}_0) \delta(\boldsymbol{x} - \boldsymbol{x}_0), \tag{3.35}$$

as expected. Notice that $(\partial \rho q / \partial p_0)_{p,\phi} = 1/q$ so that $\partial_s q^{-2} = \partial_s [(1/q)(\partial \rho q / \partial p_0)_{p,\phi}] = \rho \, \partial_s \tilde{m}$, where $\tilde{m}$ is the linearized mass flux perturbation defined in Giles & Pierce (1997), and thus the first integral on the right-hand side of (3.34) is actually the integral derived in Giles & Pierce (1997). The second integral also has an analogue in the compressible case, so the solution shown in Giles & Pierce (1997) is apparently incomplete.

For pressure-based functionals, the first term in (3.34) does not contribute to the linearized functional, which can then be written as

$$I^{(3)}(\boldsymbol{x}_0) = -\int_0^\infty \mathrm{d}s \partial_s q^{-2}(\boldsymbol{x}(s)) I^{(1)}(\boldsymbol{x}(s)) + \int_0^\infty \mathrm{d}s \frac{2}{q^2} \partial_s \phi(\boldsymbol{x}(s)) I^{(2)}(\boldsymbol{x}(s)). \tag{3.36}$$

Again, the first integral on the right-hand side of (3.36) is equivalent to the corresponding integral in Giles & Pierce (1997), where it was used to argue that there is a potential divergence along the incoming stagnation streamline. Whether this singularity is actually present or not depends on the cost function and the flow conditions. Numerical tests show that lift-adjoint solutions seem to have these singularities even in incompressible and irrotational flow, while drag-adjoint solutions only show them in certain transonic cases (Lozano & Ponsin 2021*b*).

https://doi.org/10.1017/jfm.2022.415 Published online by Cambridge University Press

We can now substitute (3.17) and (3.22) into (3.36) to compute the linearized functional corresponding to the stagnation pressure point perturbation (3.34). For drag, we get

$$I_D^{(3)} = -\frac{1}{q^2 q_\infty c_\infty}(\boldsymbol{v} - \boldsymbol{v}_\infty)^2, \tag{3.37}$$

while for lift, the result is

$$I_L^{(3)}(\boldsymbol{x}_0) = -\frac{2}{q^2 c_\infty}(u \sin\alpha - v\cos\alpha) + \frac{q_\infty}{c_\infty}\Xi, \tag{3.38}$$

where

$$\Xi = -\int_0^\infty \mathrm{d}s \partial_s q^{-2}(\boldsymbol{x}(s))\Upsilon^{(1)}(\boldsymbol{x}(s)) + 2\int_0^\infty \mathrm{d}s \frac{1}{q^2}\partial_s\phi(\boldsymbol{x}(s))(1+\Upsilon^{(2)}(\boldsymbol{x}(s))), \tag{3.39}$$

and

$$\left.\begin{aligned} \Upsilon^{(1)}(z) &= -i\left(\frac{\zeta_{te}-\zeta_0}{\zeta(z)-\zeta_{te}} - \frac{\overline{\zeta_{te}}-\overline{\zeta_0}}{\overline{\zeta}(z)-\overline{\zeta_{te}}}\right) \\ &= 2\frac{X_{te}(Y_0-Y)+X_0(Y-Y_{te})+X(Y_{te}-Y_0)}{(X-X_{te})^2+(Y-Y_{te})^2}, \\ \Upsilon^{(2)}(z) &= \frac{\zeta_{te}-\zeta_0}{\zeta(z)-\zeta_{te}} + \frac{\overline{\zeta_{te}}-\overline{\zeta_0}}{\overline{\zeta}(z)-\overline{\zeta_{te}}} \\ &= 2\frac{(X-X_0)(X-X_{te})+(Y-Y_0)(Y-Y_{te})-(X-X_{te})^2-(Y-Y_{te})^2}{(X-X_{te})^2+(Y-Y_{te})^2}. \end{aligned}\right\} \tag{3.40}$$

In (3.39), the integration is carried out along the streamline downstream of $\boldsymbol{x}_0$. Finally, X and Y in (3.40) are the Cartesian coordinates on the circle plane, in terms of which $\zeta = X + iY$.

4. Analytic adjoint solutions

Using (3.5), (3.8), (3.17), (3.20), (3.22), (3.27), (3.37) and (3.38), we can compute the analytic adjoint solutions as

$$\begin{aligned} (\psi_1, \psi_2, \psi_3) &= (I^{(1)}, I^{(2)}, I^{(3)}) \begin{pmatrix} 1 & 0 & q^{-2} \\ u & v & 2q^{-2}u \\ v & -u & 2q^{-2}v \end{pmatrix}^{-1} \\ &= (I^{(1)}, I^{(2)}, I^{(3)}) \begin{pmatrix} 2 & -q^{-2}u & -q^{-2}v \\ 0 & q^{-2}v & -q^{-2}u \\ -q^2 & u & v \end{pmatrix}. \end{aligned} \tag{4.1}$$

For drag, we get

$$\begin{pmatrix} \psi_1 \\ \psi_2 \\ \psi_3 \end{pmatrix}_{Drag} = \frac{1}{c_\infty q_\infty}\begin{pmatrix} q^2 - q_\infty^2 \\ q_\infty\cos\alpha - u \\ q_\infty\sin\alpha - v \end{pmatrix}, \tag{4.2}$$

which is exactly the analytic drag adjoint solution found in Lozano & Ponsin (2021*a*). It can be checked that it obeys the adjoint equation and boundary conditions.

https://doi.org/10.1017/jfm.2022.415 Published online by Cambridge University Press

Notice that no assumption has been made about the lift of the base flow solution. Hence, this two-dimensional solution should be valid for lifting and non-lifting flows alike, contrary to what was claimed in Lozano & Ponsin (2021*a*), where the validity of the solution was restricted to non-lifting flows based on far-field behaviour. In 2-D, incompressible flow past a lifting airfoil is still irrotational. The only difference between a lifting and a non-lifting flow is in the order of the subleading terms as $r \to \infty$

$$\left.\begin{aligned} \boldsymbol{v} &= \boldsymbol{v}_\infty + O(1/r^2) \quad (\textit{non - lifting}), \\ \boldsymbol{v} &= \boldsymbol{v}_\infty + O(1/r) \quad (\textit{lifting}). \end{aligned}\right\} \tag{4.3}$$

Adjoint boundary condition at the outer boundary demands

$$\int_{S_\infty} \psi^T \hat{n} \cdot \boldsymbol{A}\delta U \, \mathrm{d}s = 0, \tag{4.4}$$

for perturbations δU respecting the far-field state. For incompressible flow, we have

$$\psi_{drag}^T \hat{n} \cdot \boldsymbol{A}\delta U = \frac{\rho q_\infty \Gamma_0}{2\pi r}(\delta u \sin\alpha - \delta v \cos\alpha) + O(1/r^2), \tag{4.5}$$

where Γ_0 is the circulation of the base flow, so if δu, δv tend to zero at the far-field (which is a reasonable assumption as otherwise the free stream state would be perturbed), then the above term is at least $O(1/r^2)$ and the far-field integral vanishes, thus guaranteeing that ψ_{drag} is also a valid solution for lifting flows. The discrepancies observed in Lozano & Ponsin (2021*a*) can then be attributed to the dependence of the numerical solution on the distance from the body to the far-field (20 chord lengths for the meshes used in Lozano & Ponsin 2021*a*).

However, for lift, we get the result

$$\begin{pmatrix} \psi_1 \\ \psi_2 \\ \psi_3 \end{pmatrix}_{Lift} = \frac{q_\infty}{c_\infty} \begin{pmatrix} 2\Upsilon^{(1)} - q^2\Xi \\ -\dfrac{\sin\alpha}{q_\infty} + u\Xi - \dfrac{u}{q^2}\Upsilon^{(1)} + \dfrac{v}{q^2}(1+\Upsilon^{(2)}) \\ \dfrac{\cos\alpha}{q_\infty} + v\Xi - \dfrac{v}{q^2}\Upsilon^{(1)} - \dfrac{u}{q^2}(1+\Upsilon^{(2)}) \end{pmatrix}. \tag{4.6}$$

It can be checked (with a long derivation that can be conveniently alleviated with a symbolic manipulation software) that (4.6) obeys the adjoint equations, for which one needs to use the following identities:

$$\left.\begin{aligned} \partial_x \Upsilon^{(2)}(z) &= \partial_y \Upsilon^{(1)}(z), \\ \partial_y \Upsilon^{(2)}(z) &= -\partial_x \Upsilon^{(1)}(z), \end{aligned}\right\} \tag{4.7}$$

which follow from the holomorphicity of $\Upsilon^{(2)}(z) + i\Upsilon^{(1)}(z)$, as well as

$$\boldsymbol{v} \cdot \nabla \Xi = q\partial_s q^{-2}\Upsilon^{(1)} - q\frac{2}{q^2}\partial_s\phi(1+\Upsilon^{(2)}) = -\frac{2}{q^3}\Upsilon^{(1)}\boldsymbol{v}\cdot\nabla q - \frac{2}{q^2}\boldsymbol{v}\cdot\nabla\phi(1+\Upsilon^{(2)}), \tag{4.8}$$

and the incompressibility and irrotationality of the base flow. Likewise, (4.6) also obeys the wall boundary conditions,

$$\begin{aligned} c_\infty(\boldsymbol{\varphi}\cdot\hat{n}) = c_\infty(n_x\psi_2 + n_y\psi_3) &= (-\sin\alpha, \cos\alpha)\cdot\hat{n} + q_\infty(\boldsymbol{v}\cdot\hat{n})(\Xi - q^{-2}\Upsilon^{(1)}) \\ &+ \frac{q_\infty}{q^2}(1+\Upsilon^{(2)})(v, -u)\cdot\hat{n} = (-\sin\alpha, \cos\alpha)\cdot\hat{n}, \end{aligned} \tag{4.9}$$

since $\boldsymbol{v}\cdot\hat{n} = 0$ and $1 + \Upsilon^{(2)} = 0$ at the wall.

https://doi.org/10.1017/jfm.2022.415 Published online by Cambridge University Press

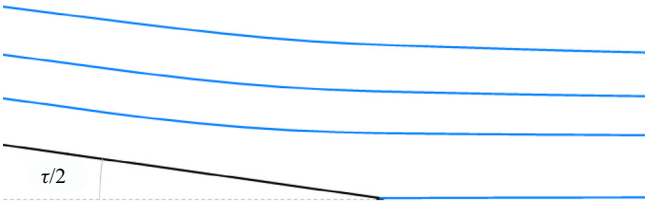


Figure 1. Streamlines for potential flow past a wedge of angle τ.

4.1. *Behaviour of* Ξ

The streamline integral equation (3.39) represents the contribution to lift, due to the Kutta condition, of a unit point perturbation to the stagnation pressure. This perturbation generates secondary point sources and vortices along the streamline downstream of the insertion point. The contributions of these secondary perturbations to the lift (see (3.17), (3.22)) diverge near the trailing edge, which gives rise to a singular behaviour of Ξ near the dividing streamline upstream of the trailing edge or rear stagnation point (which includes the wall and the incoming stagnation streamline). Along the stagnation streamline upstream of the body, the integral is not defined, as the streamline splits up in two at the stagnation point, while along the wall, the integral diverges. For a circle, for example, the integral along the wall is

$$\Xi(\boldsymbol{x}_0) \sim \int_0^{\theta_0} \mathrm{d}\theta \cos^2(\theta/2)\cot\theta \csc^3\theta, \tag{4.10}$$

where $\boldsymbol{x}_0 = (R\cos\theta_0, R\sin\theta_0)$, which diverges as θ^{-3} at the rear stagnation point ($\theta = 0$). Away from the dividing streamline, the integral grows unbounded as the corresponding streamline approaches the dividing streamline. To investigate the character of the divergence, we consider a simplified setup involving flow past a wedge of half-angle $\tau/2$ (figure 1).

The asymptotic form of the complex potential for this case is $z^{2/k}$, where $k = 2 - \tau/\pi$, so that stream function reads, in polar coordinates, $\psi = r^{2/k}\sin(2\theta/k)$, from which it follows that the minimum distance from a particular streamline to the trailing edge is $r_{min} \sim \psi^{k/2}$, while the distance from a given point on the streamline to the dividing streamline is $d \sim \psi \sim r_{min}^{2/k}$. Likewise, the flow speed behaves as $q = O(r^{2/k-1})$, so $\partial_s q = O(r^{2/k-2})$, and likewise $\partial_s\phi = O(r^{-1})$. Finally, $\zeta \sim z^{1/k}$ and, thus, $\Upsilon^{(1)} = O(r^{-1/k})$ and $\Upsilon^{(2)} = O(r^{-1/k})$, so integrating along a streamline,

$$\Xi \sim r_{min}^{2-5/k} \sim r_{min}^{-(2\tau/\pi+1)/(2-\tau/\pi)}, \tag{4.11}$$

which depends on the trailing edge wedge angle τ. Notice that the exponent is always negative for $0 < \tau \leq \pi$. It is thus clear that Ξ has a potential divergence as the streamline approaches the dividing streamline. Let us consider three different scenarios in terms of the relative position of $\boldsymbol{x}_0$.

(1) In case 1, $\boldsymbol{x}_0$ is approaching the rear singularity (trailing edge or rear stagnation point). As $\boldsymbol{x}_0$ approaches the rear singularity (figure 2), the distance to the rear singularity behaves as $r \sim r_{min}$ asymptotically. Hence, $\Xi(\boldsymbol{x}_0)$ diverges as $r^{2-5/k} \sim r^{-(2\tau/\pi+1)/(2-\tau/\pi)}$ as $\boldsymbol{x}_0$ approaches the rear singularity. This singular behaviour had been already anticipated (including the dependence on the trailing edge angle) in Giles & Pierce (1997), but no concrete predictions were made for the exponent.

https://doi.org/10.1017/jfm.2022.415 Published online by Cambridge University Press

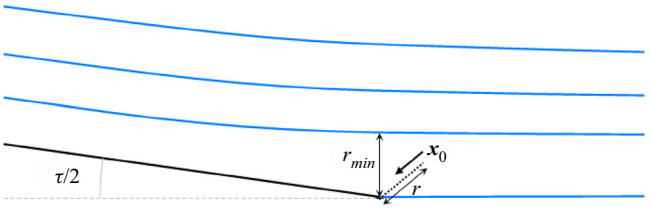


Figure 2. Set-up for case 1.

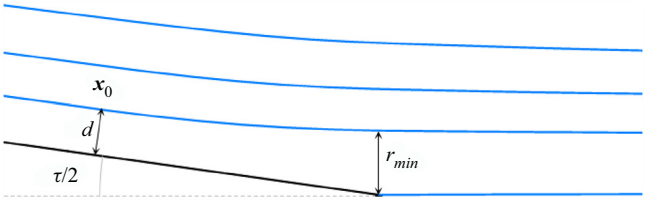


Figure 3. Set-up for case 2.

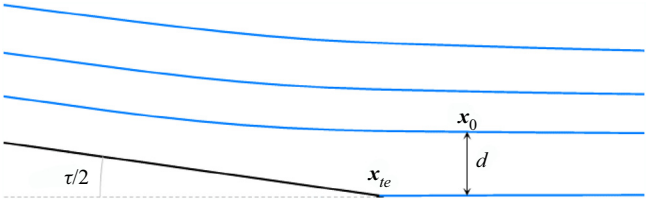


Figure 4. Set-up for case 3.

A $1/r_{min}$ singularity at the rear stagnation point was predicted in Lozano & Ponsin (2021*b*) for blunt bodies in potential flow using the form of the streamline integral derived in Giles & Pierce (1997), while the actual value for this case (for which $\tau = \pi \Rightarrow k = 1$) is $\Xi \sim r^{-3}$.

(2) In case 2, $\boldsymbol{x}_0$ is upstream of the rear singularity (figure 3). As $\boldsymbol{x}_0$ approaches the dividing streamline upstream of the rear singularity, $\Xi(\boldsymbol{x}_0)$ diverges as $r_{\min}^{2-5/k} \sim d^{k-5/2} \sim 1/d^{\tau/\pi+1/2}$, where d is the distance from $\boldsymbol{x}_0$ to the dividing streamline (incoming stagnation streamline or wall). Notice that the singularity exponent is not universal since it depends on the trailing edge angle τ, and reduces to the inverse square-root behaviour predicted in Giles & Pierce (1997) for cusped trailing edges (for which $\tau = 0$).

(3) In case 3, as $\boldsymbol{x}_0$ approaches the rear stagnation streamline downstream of the rear singularity (figure 4), $\Xi(\boldsymbol{x}_0)$ does not diverge (the minimum distance from the streamline to the trailing edge is now $|\boldsymbol{x}_0 - \boldsymbol{x}_{te}|$, which is always greater than zero) but rather behaves as $\Xi(\boldsymbol{x}_0) \sim d$, where d is the distance from $\boldsymbol{x}_0$ to the dividing streamline.

The results of this asymptotic analysis are confirmed by actual computations (see § 5). This suggests that the origin of the divergence along the dividing streamline is the singularity at the trailing edge/rear stagnation point. This can be put on a firmer basis by noting that, as it will be shown later on, while the integral does get a small contribution from the leading-edge region, it is very approximately constant upstream of the rear

https://doi.org/10.1017/jfm.2022.415 Published online by Cambridge University Press

singularity and vanishingly small downstream. Likewise, the integral behaves in exactly the same fashion at both the incoming stagnation streamline and the wall, with an exponent that depends on the local geometry around the rear singularity.

4.1.1. *Influence of Ξ on the sensitivity derivatives and the adjoint boundary conditions*
The divergences of Ξ (and $\Upsilon^{(1)}$ and $\Upsilon^{(2)}$) are propagated to the lift-based adjoint variables (4.6). However, two linear combinations of the adjoint variables,

$$\left.\begin{aligned} I^{(1)} &= \psi_1 + \boldsymbol{v}\cdot(\psi_2,\psi_3) = (q_\infty \Upsilon^{(1)} - u\sin\alpha + v\cos\alpha)/c_\infty, \\ I^{(2)} &= v\psi_2 - u\psi_3 = (-v\sin\alpha - u\cos\alpha + q_\infty(1+\Upsilon^{(2)}))/c_\infty, \end{aligned}\right\} \tag{4.12}$$

which yield the linearized perturbations to the lift due to a point source and a point vortex, respectively (Giles & Pierce 1997), remain finite except at the trailing edge. This fact is relevant since the adjoint variables enter the (continuous) adjoint-based sensitivity derivatives (2.12) precisely through $I^{(1)}$, which protects the sensitivities from diverging with mesh refinement (a fact that is well established numerically, see e.g. Lozano 2012, 2017, 2019*b*; Lozano & Ponsin 2022). Likewise, $I^{(2)}$ approaches $q\hat{n}_S\cdot(\psi_2,\psi_3)$ as the point approaches the wall and is thus directly related to the adjoint boundary condition, which is thus respected by the analytical solution and protected upon mesh refinement (Lozano 2019*b*). Finally, the divergence along the dividing streamline is encapsulated into a third (linearly independent) combination

$$I^{(3)} = (\psi_1 + 2u\psi_2 + 2v\psi_3)/q^2 = (q_\infty \Xi - 2q^{-2}u\sin\alpha + 2q^{-2}v\cos\alpha)/c_\infty, \tag{4.13}$$

which yields the linearized perturbation to the lift due to a unit stagnation pressure point perturbation.

It is important to point out, however, that the above split of the adjoint solution space into protected and unprotected terms (as regards the dividing streamline singularity) is arbitrary and based on our choice of point perturbations (inherited from Giles & Pierce 1997). In fact, it turns out that any linear combination

$$a\psi_1 + b\psi_2 + c\psi_3, \tag{4.14}$$

which corresponds to a point perturbation with source vector $f = (a,b,c)^T$, obeying $-aq^2 + bu + cv = 0$, does not contain the streamline integral Ξ and is thus protected from the dividing streamline singularity. Conversely, if $-aq^2 + bu + cv \neq 0$, then the corresponding perturbation is singular along the dividing streamline. One such example is $f = (0,u,v)^T$, which is related to the drag Eulerlet (Chadwick *et al.* 2019), a Green's function of the incompressible Euler equations linearized around a uniform flow which carries one unit of drag.

5. Sample solutions

To illustrate the results presented above, we present now the results of direct evaluation of the adjoint analytical solutions in two cases: blunt body (a circle) and an airfoil with a sharp non-cusped trailing edge.

5.1. *Circle*

As explained above, obtaining meaningful adjoint solutions for bodies without sharp trailing edges, such as the circle, requires a Kutta condition to guarantee that the

https://doi.org/10.1017/jfm.2022.415 Published online by Cambridge University Press

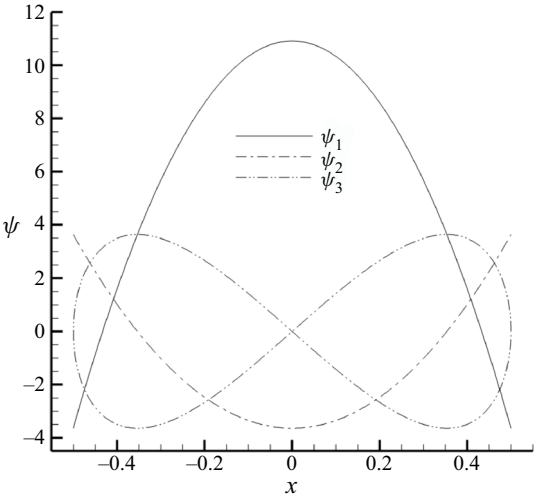


Figure 5. Analytic drag-based adjoint solution at the wall for incompressible, inviscid flow past a circle with $\Gamma_0 = 0$.

perturbations preserve the location of the rear stagnation point. As a consequence of this fact, the solutions (4.2) and (4.6) are applicable here, resulting in the analytic drag-based adjoint solution shown in figure 5.

Here and in what follows, the normalization of the adjoint variables is given by (4.2) and (4.6). For the flow variables, dimensions are fixed such that $\rho_\infty = 1 = q_\infty$, while spatial coordinates are normalized with the reference length ℓ (the diameter of the circle in this case).

To obtain the analytic lift-based adjoint solution, the streamline integral $\Xi(\boldsymbol{x}_0)$ has to be evaluated at each point of the domain. As with Giles and Pierce's analytic quasi-1-D adjoint solution (Giles & Pierce 2001), this cannot be done in analytic form in general, so the solution has to be evaluated numerically instead. In the present case, there is the additional complication that the integration requires prior determination of the streamline passing through $\boldsymbol{x}_0$. Thus, to produce sample solutions, a numerical procedure must be assembled to trace the streamline and perform the integration. Streamline tracing is carried out by direct numerical integration of the equation $\mathrm{d}\boldsymbol{x}/\mathrm{d}t = \boldsymbol{v}(\boldsymbol{x})$ with a fourth-order Runge–Kutta method (see e.g. Giles & Haimes 1990). The integration is carried out concurrently with a simple trapezoidal rule. Contour maps of the analytic lift-adjoint solution obtained in this way are shown in figure 6, while figure 7 shows the adjoint solution along three vertical lines crossing the stagnation streamline upstream and downstream of the circle and impinging the wall as indicated in figure 6. It is clear from both figures that the solution is singular along the dividing streamline upstream of the rear stagnation point (the circle wall and the incoming stagnation streamline), but not across the rear stagnation streamline.

These singularities are caused by the streamline integral Ξ. In § 4, we argued that the streamline integral behaves as $\Xi \sim r_{min}^{2-5/k} \sim r_{min}^{-(2\tau/\pi+1)/(2-\tau/\pi)}$ in terms of the distance of the streamline to the rear stagnation point/trailing edge. Since $k = 1$ for the circle, we expect that $\Xi \sim r_{min}^{-3}$ at the rear stagnation point and $\Xi \sim d^{-3/2}$ at the wall and the incoming stagnation streamline, which is confirmed in figures 8–10. Figure 8 plots the value of the integral Ξ at several points placed along a vertical line crossing the incoming

https://doi.org/10.1017/jfm.2022.415 Published online by Cambridge University Press

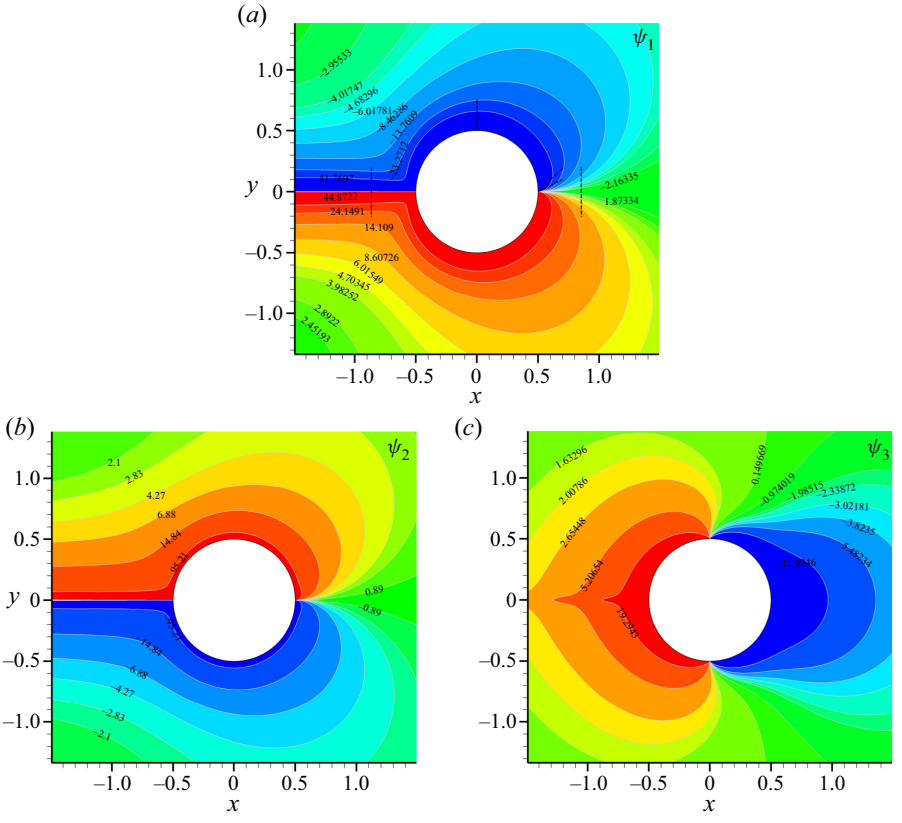


Figure 6. Analytic lift-based adjoint solution for incompressible, inviscid flow past a circle: (*a*) ψ_1; (*b*) ψ_2; (*c*) ψ_3.

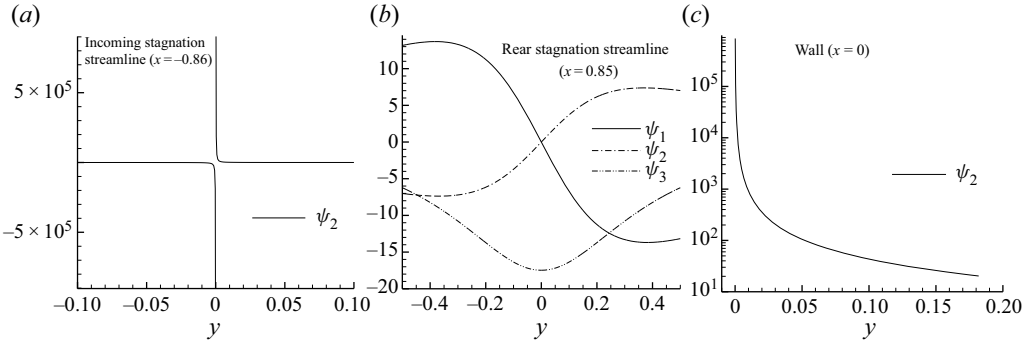


Figure 7. Analytic adjoint solution along vertical lines crossing the stagnation streamline upstream and downstream of the circle and impinging the wall as indicated in figure 6.

stagnation streamline (the x axis) as indicated in figure 6. This value is fitted against the distance d to the stagnation streamline, yielding $\Xi \sim d^{-1.47}$, which is close to the theoretical prediction and to the value $\Xi \sim d^{-1.46}$ obtained at the wall (figure 9), but also against the minimum distance of the streamline to the rear stagnation point r_{min}, yielding $\Xi \sim r_{min}^{-2.9}$, which is close to the theoretical value and to the value of the exponent obtained

https://doi.org/10.1017/jfm.2022.415 Published online by Cambridge University Press

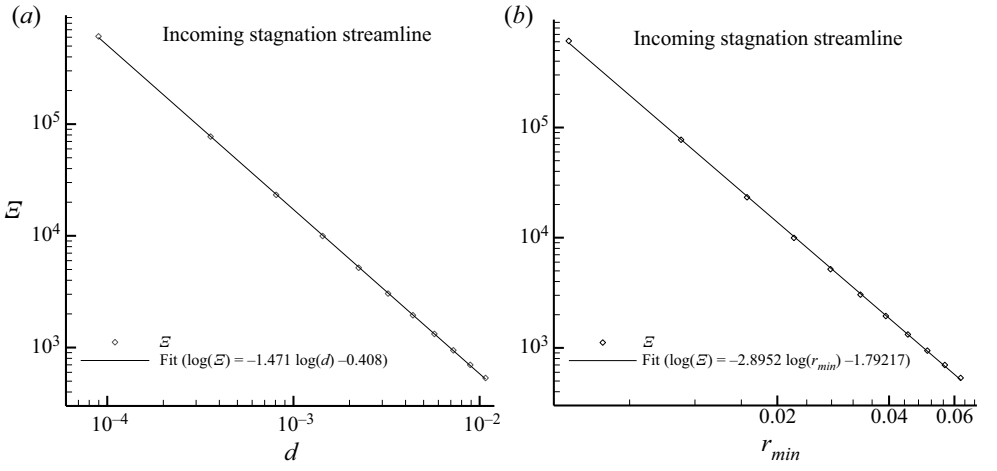


Figure 8. Value of the streamline integral computed with the analytic solution along a vertical line at $x = -0.86$ crossing the stagnation streamline upstream of the circle as indicated in figure 6. (*a*) Values of Ξ versus distance d to the stagnation streamline. (*b*) Values of Ξ versus minimum distance r_{min} of the streamline to the rear stagnation point.

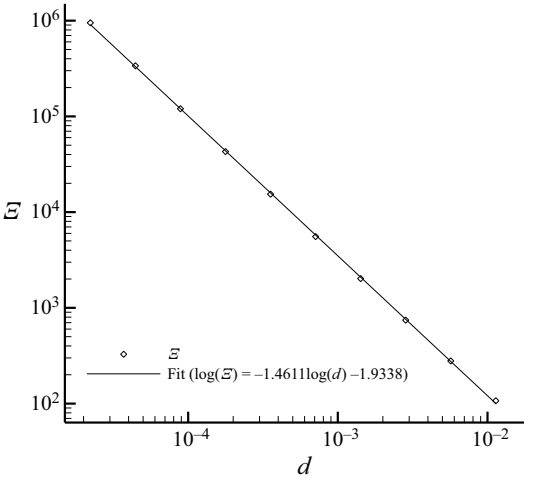


Figure 9. Value of the streamline integral computed with the analytic solution along the vertical line $x = 0$ impinging the circle wall as indicated in figure 6.

for the rear stagnation point (figure 10). Finally, the integral vanishes linearly $\Xi \sim d$ across the rear stagnation streamline (figure 11), which is not singular.

We have argued above that the behaviour at the wall and stagnation streamline is essentially governed by the singularity exponent at the rear singularity, which is thus the primary singularity. The results in figures 8 and 9 do support this idea, which is further illustrated with figures 12 and 13. Figure 12(*a*) shows the value of Ξ along the streamlines shown on the right plot. It can be clearly seen that the integral is quite approximately constant upstream of the trailing edge region and negligible downstream, and that the upstream value grows as the streamline approaches the dividing streamline (the downstream value, however, approaches zero), as expected. Figure 13, which focuses on the outermost streamline of figure 12, plots the running value of Ξ along the streamline, as well as $I = -\partial_s q^{-2}\Upsilon^{(1)} + 2q^{-2}\partial_s\phi(1 + \Upsilon^{(2)})$, which is the integrand in Ξ. It is clear

https://doi.org/10.1017/jfm.2022.415 Published online by Cambridge University Press

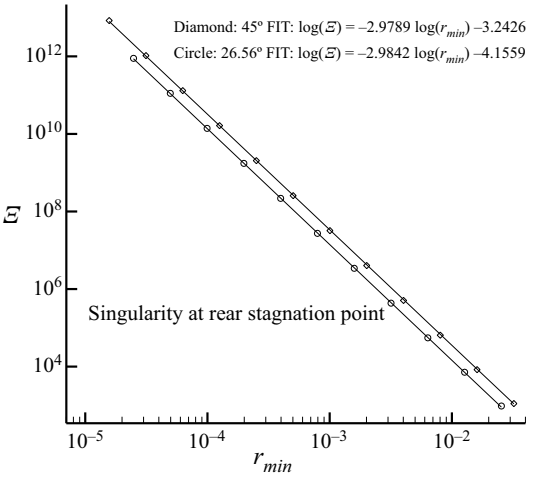


Figure 10. Value of the streamline integral computed with the analytic solution along two lines approaching the rear stagnation point with different inclinations as indicated in figure 6.

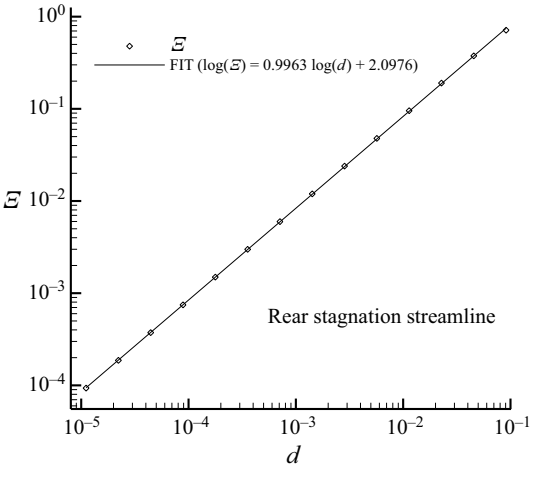


Figure 11. Value of the streamline integral computed with the analytic solution along a vertical line at $x = 0.85$ crossing the stagnation streamline downstream of the circle as indicated in figure 6.

that the main contribution to the integral comes from the region near the rear stagnation point, with a negligible contribution from the leading-edge region.

Finally, figure 14 plots the value of the linearized functionals $I^{(1)} = \psi_1 + \boldsymbol{v} \cdot (\psi_2, \psi_3)$ and $I^{(2)} = v\psi_2 - u\psi_3$ on the circle wall. These quantities have a finite value throughout the wall (except $I^{(1)}$, which diverges at the trailing edge), as expected.

5.2. *Airfoil with finite trailing-edge angle*

The second case involves incompressible, inviscid flow at an angle of attack $\alpha = 0°$ past a symmetrical van de Vooren airfoil given by the conformal transformation (Katz & Plotkin

https://doi.org/10.1017/jfm.2022.415 Published online by Cambridge University Press

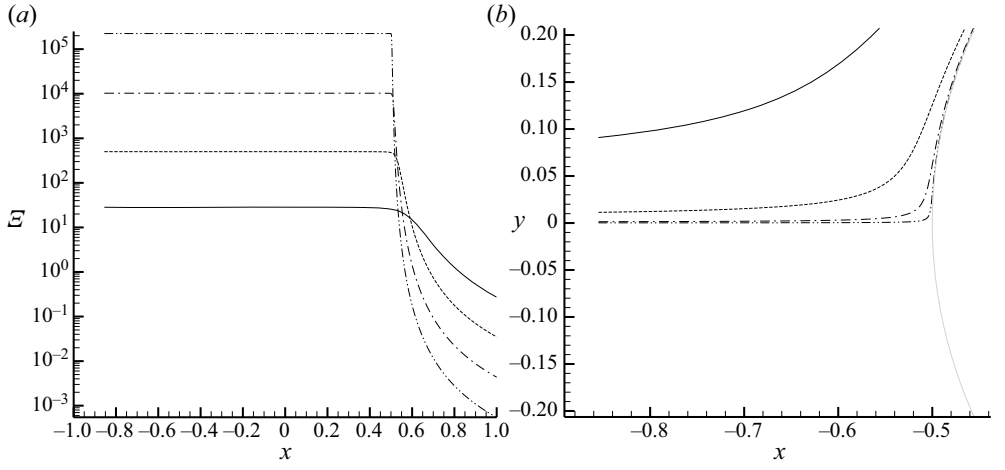


Figure 12. (*a*) Running value of $\Xi(\boldsymbol{x}_0)$ along the streamlines indicated in panel (*b*). The forward and rear stagnation points are located at $x = -0.5$ and $x = 0.5$, respectively.

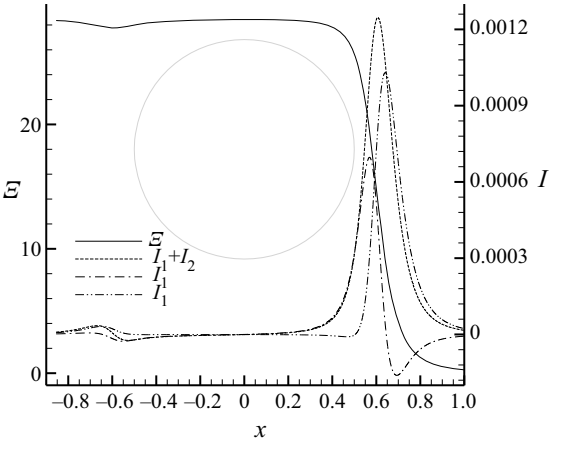


Figure 13. Running value of $\Xi(\boldsymbol{x})$ and integrands $I_1 = -\partial_s q^{-2}\Upsilon^{(1)}$, $I_2 = 2\partial_s\phi(1+\Upsilon^{(2)})/q^2$ and $I = I_1 + I_2$ along the outermost streamline of figure 12. The extension of the circle is indicated for reference purposes.

2001):

$$z = \frac{(\zeta - R)^k}{(\zeta - \varepsilon R)^{k-1}} + 1, \tag{5.1}$$

where $R = (1+\varepsilon)^{k-1}/2^k$, ε is a thickness parameter and k is related to the trailing-edge angle τ as $k = 2 - \tau/\pi$. The transformation (5.1) maps the airfoil in the z plane to a circle of radius R centred at the origin in the ζ plane. In this paper, we set $\varepsilon = 0.0371$ and $k = 86/45$, resulting in an airfoil with 12 % thickness and finite trailing edge angle $\tau = 16^\circ$ that is shown in figure 15, where the analytic flow solution obtained with conformal transformation techniques is also depicted. The analytic flow solution can be found in Katz & Plotkin (2001) and can be obtained from the solution in the circle plane (3.10) and the transformation (5.1) as $(u - iv)_{airfoil} = (\mathrm{d}\Phi/\mathrm{d}\zeta)/(\mathrm{d}z/\mathrm{d}\zeta)$.

https://doi.org/10.1017/jfm.2022.415 Published online by Cambridge University Press

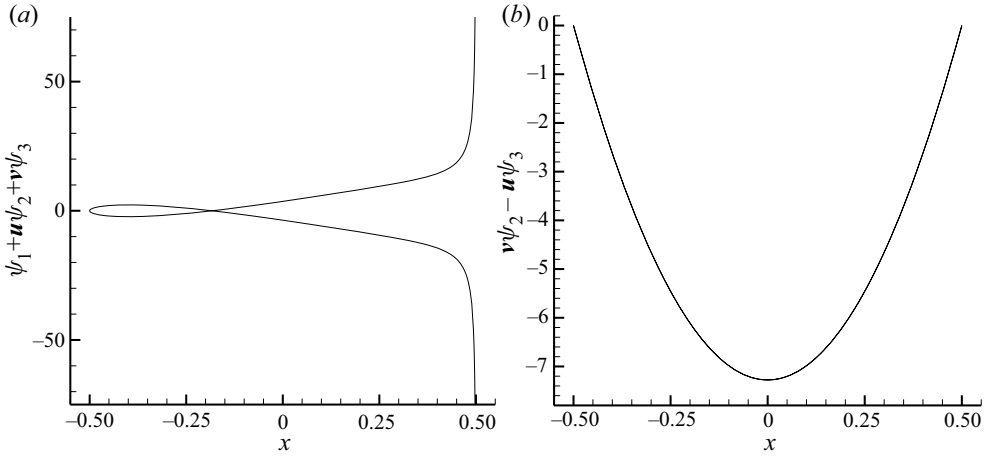


Figure 14. $I^{(1)} = \psi_1 + \boldsymbol{v} \cdot (\psi_2, \psi_3)$ and $I^{(2)} = v\psi_2 - u\psi_3$ at the wall computed with the analytic lift-based adjoint solution for incompressible, inviscid flow past a circle.

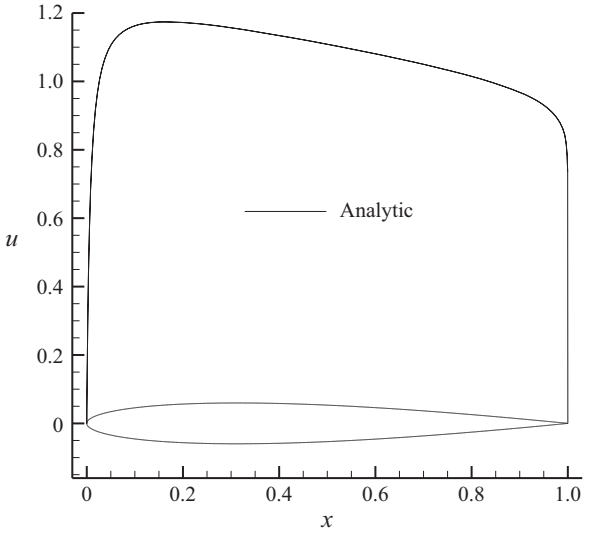


Figure 15. Geometry and analytic x-velocity for incompressible, inviscid flow at $\alpha = 0°$ past a van de Vooren airfoil with trailing-edge angle $\tau = 16°$ and 12 % thickness computed with conformal transformation techniques. The flow is normalized such that $\rho_\infty = 1 = q_\infty$ and the airfoil profile is shown for reference.

Using this analytic flow solution, the corresponding analytic adjoint solutions can be computed using (4.2) and (4.6). Figure 16 shows the analytic drag-based adjoint solution. This solution has been compared to numerical solutions obtained by discretizing the adjoint equation directly in Lozano & Ponsin (2021*a*, 2022).

As for lift, the computation of the analytic adjoint solution is carried out with the fourth-order Runge–Kutta integrator described above. The streamline tracing is performed in the circle plane and then translated into the airfoil plane via the conformal transformation (5.1). Contour maps of the analytic lift adjoint solution obtained in this way are shown in figure 17. Again, a comparison of this solution to numerical adjoint solutions can be found in Lozano & Ponsin (2022).

https://doi.org/10.1017/jfm.2022.415 Published online by Cambridge University Press

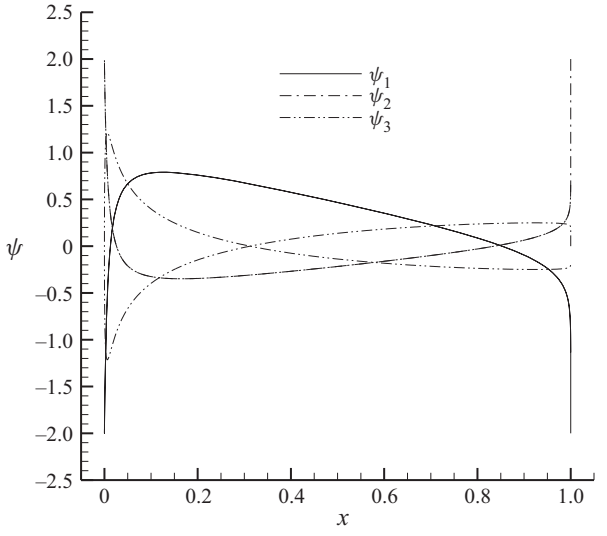


Figure 16. Analytic drag-based adjoint solution on the airfoil profile for incompressible, inviscid flow at $\alpha = 0°$ past a van de Vooren airfoil with trailing-edge angle $\tau = 16°$ and 12 % thickness.

As in the circle case, the analytic solution shows singularities at the wall, across the incoming stagnation streamline and at the trailing edge, but not across the rear stagnation streamline. This is more clearly illustrated in figures 18–21, which plot the streamline integral Ξ along lines approaching the stagnation streamline upstream of the airfoil, the wall, the trailing edge and the rear stagnation streamline, respectively, as indicated in figure 17. In all cases, the behaviour of the integral has been illustrated by fitting the curves to a power of the distance to the dividing streamline or the trailing edge as appropriate. At both the incoming stagnation streamline and the wall, the integral diverges as roughly $1/d^{0.58}$, where d is the distance to the stagnation streamline or to the wall. Noting that $k = 86/45$ for the present case, the exponent is close to the theoretical prediction $\Xi \sim 1/d^{53/90} = 1/d^{0.589}$. At the trailing edge, the integral shows a $1/r^{0.61}$ singularity (where r is the distance to the trailing edge) regardless of the inclination of the line, which is again in agreement with the theoretical prediction $\Xi \sim 1/r^{53/86} = 1/r^{0.616}$. Finally, the streamline integral vanishes as $\Xi \sim d$ at the stagnation streamline downstream of the trailing edge.

Figure 22 shows the value of $I = -\partial_s q^{-2}\Upsilon^{(1)} + 2q^{-2}\partial_s\phi(1 + \Upsilon^{(2)})$ along a streamline originating near the stagnation streamline upstream of the airfoil. It is clear, as in the previous case, that the main contribution to the integral comes from the region near the trailing edge, with a negligible contribution from the leading-edge region.

To end the analysis of the airfoil solution, figure 23 focuses on the behaviour of the adjoint solution near the airfoil profile. In the plot, the first component of the analytic adjoint solution is shown for a succession of O-shaped curves surrounding the van der Vooren airfoil profile and progressively closer to it, clearly demonstrating the divergence of the analytic solution at the wall. It is clear that the anomaly observed in numerical computations (Lozano 2019*b*; Lozano & Ponsin 2022; Peter *et al.* 2022) is caused by a divergence of the analytic solution at the wall. On the numerical side, the numerical viscosity of the solver stabilizes the divergence, producing a finite value at the profile which nevertheless varies continually as the grid spacing or the intensity of the numerical dissipation change (Lozano & Ponsin 2021*b*). At any rate, while the adjoint variables

https://doi.org/10.1017/jfm.2022.415 Published online by Cambridge University Press

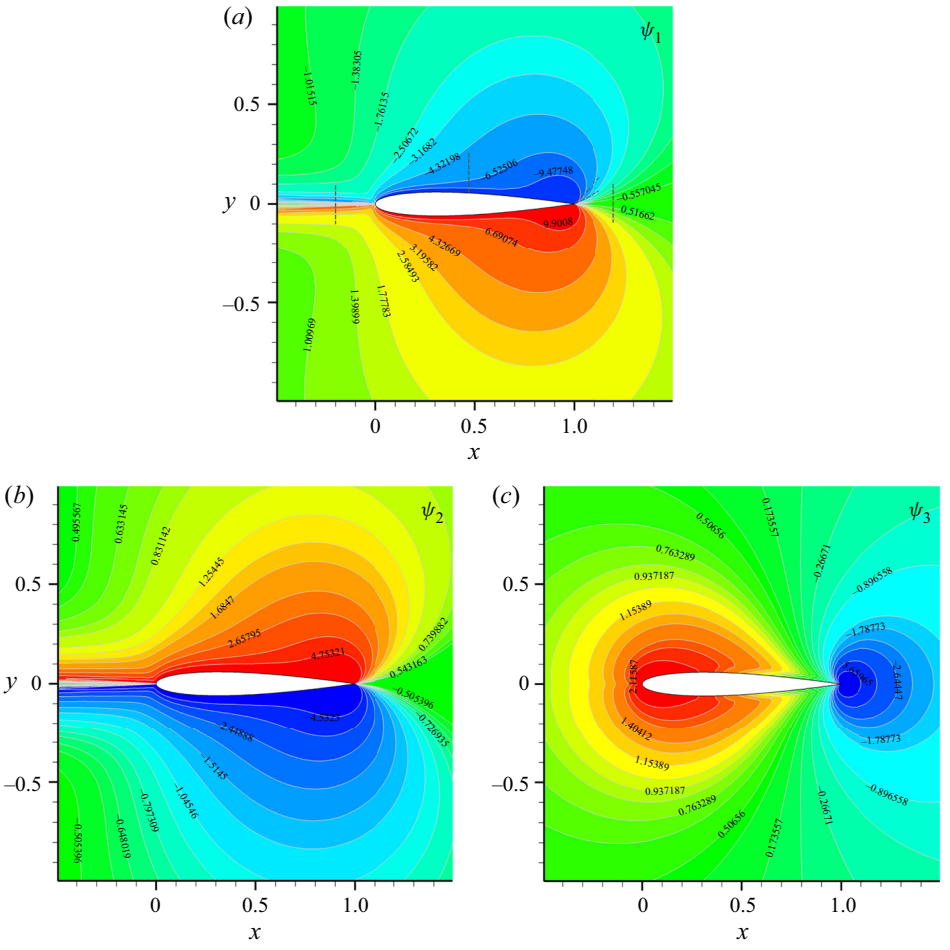


Figure 17. Analytic lift-based adjoint solution for incompressible, inviscid flow at $\alpha = 0°$ past a van de Vooren airfoil with trailing-edge angle $\tau = 16°$ and 12 % thickness: (*a*) ψ_1; (*b*) ψ_2; (*c*) ψ_3.

diverge at the wall, the linearized functionals $I^{(1)}$ and $I^{(2)}$ (4.12) are again finite across the profile (except $I^{(1)}$ which diverges at the trailing edge) as shown in figure 24.

6. Conclusions

In this paper, we have investigated the adjoint solutions for the two-dimensional incompressible Euler equations. By restricting to irrotational base flows, it is possible to derive a closed form solution to the adjoint equations using the Green's function approach developed by Giles & Pierce (2001). Drag-based and lift-based analytic adjoint solutions have been obtained in this way, and they should be of help as test cases for verification of numerical adjoint solvers.

The drag-based adjoint solution is smooth and has a particularly simple closed-form expression in terms of the flow variables. For the type of flows considered in this paper, drag is zero for the analytic solution and has thus no practical application for shape design. The drag-based adjoint solution is, however, non-trivial and can be used for verification purposes. Likewise, if drag fails to vanish in a discrete flow solution, the drag-adjoint

https://doi.org/10.1017/jfm.2022.415 Published online by Cambridge University Press

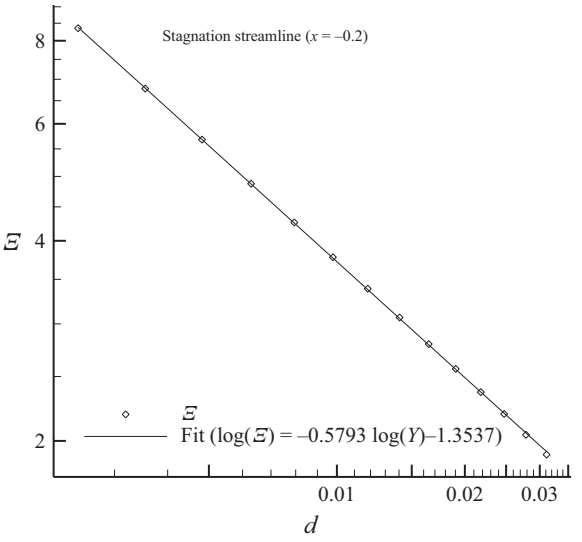


Figure 18. Value of the streamline integral computed with the analytic solution along a line crossing the stagnation streamline upstream of the airfoil as indicated in figure 17.

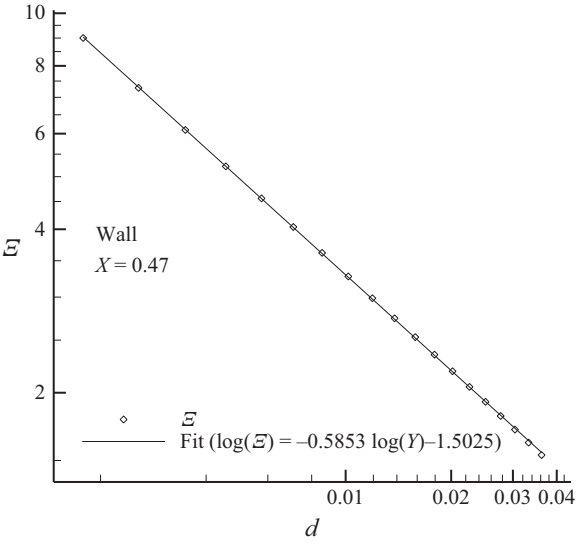


Figure 19. Value of the streamline integral computed with the analytic solution along a line impinging the airfoil as indicated in figure 17.

solution can be used to build a cheap mesh adaptation indicator that will identify those flow regions responsible for the failure, in analogous fashion to the entropy adjoint approach (Fidkowski & Roe 2010).

The lift-based adjoint solution, however, is considerably more complex, and exhibits a number of distinctive features, some of which had been already anticipated in the literature (Giles & Pierce 1997) but are now fully clarified. The lift adjoint solution shows a singularity at the trailing edge/rear stagnation point that corresponds to perturbations to the Kutta condition. The sensitivity of the Kutta condition to perturbations of the

https://doi.org/10.1017/jfm.2022.415 Published online by Cambridge University Press

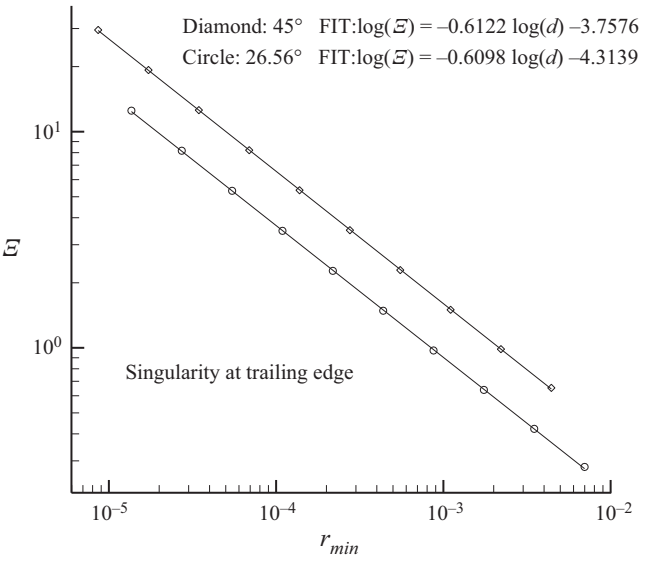


Figure 20. Value of the streamline integral computed with the analytic solution along two lines approaching the trailing edge at different inclinations as indicated in figure 17.

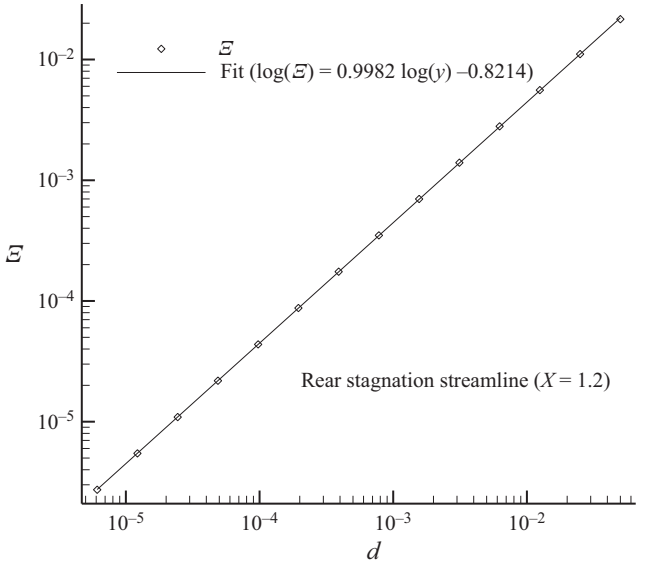


Figure 21. Value of the streamline integral computed with the analytic solution along a line crossing the stagnation streamline downstream of the airfoil as indicated in figure 17.

stagnation pressure gives rise to an additional singularity structure along the dividing streamline upstream of the rear singularity, resulting in adjoint singularities at the wall and the incoming stagnation streamline, where the adjoint solution diverges with identical exponents that nevertheless depend on the trailing edge angle. Since the analytic lift-adjoint solution is singular at walls, this finally settles the issue of the mesh divergence of inviscid adjoint solutions at solid walls (Lozano 2019*b*; Peter *et al.* 2022).

https://doi.org/10.1017/jfm.2022.415 Published online by Cambridge University Press

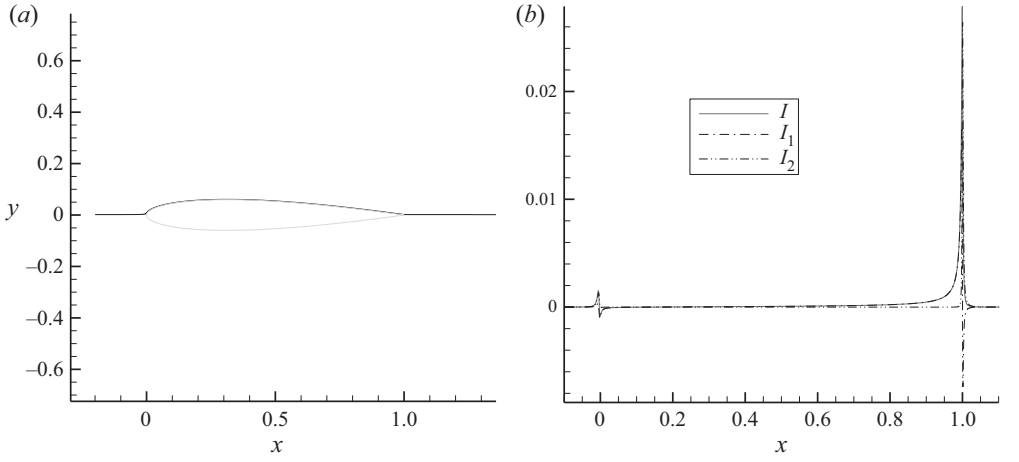


Figure 22. Plot of $I_1 = -\partial_s q^{-2}\Upsilon^{(1)}$, $I_2 = 2\partial_s\phi(1+\Upsilon^{(2)})/q^2$ and $I = I_1 + I_2$ for the streamline shown in panel (a). Inviscid, incompressible flow at $\alpha = 0°$ past a van de Vooren airfoil with trailing-edge angle $\tau = 16°$ and 12 % thickness.

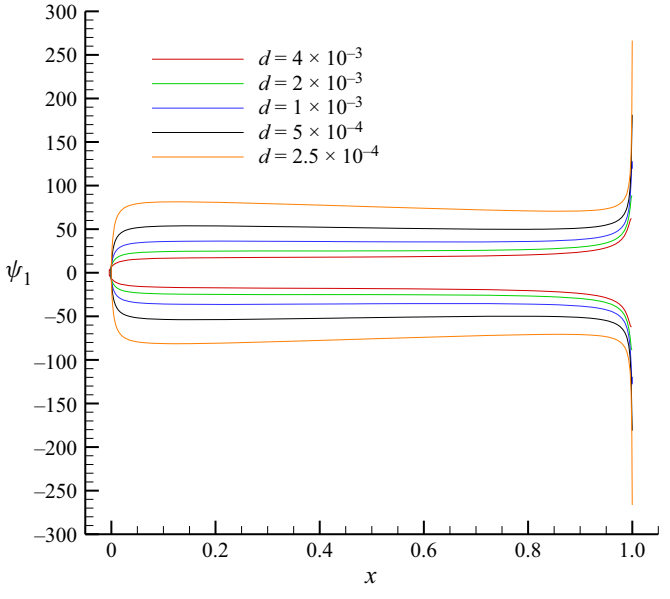


Figure 23. Analytic lift-based adjoint solution for incompressible, inviscid flow at $\alpha = 0°$ past a van de Vooren airfoil with trailing-edge angle $\tau = 16°$ and 12 % thickness on a sequence of O-shaped curves progressively approaching the airfoil.

It would be interesting to extend this analysis to compressible flow. The task was initiated in Giles & Pierce (1997), where four linearly independent source terms were defined and a preliminary analysis was carried out. However, obtaining the exact adjoint solutions would require to compute the Green's functions corresponding to these source terms or, at least, their effect on drag and lift. To the best of our knowledge, this is an open problem which appears very difficult to solve exactly, particularly for transonic flows. At any rate, preliminary analysis (Giles & Pierce 1997; Peter *et al.* 2022) shows that adjoint variables are continuous at shocks, albeit with discontinuous derivatives, and at sonic lines,

https://doi.org/10.1017/jfm.2022.415 Published online by Cambridge University Press

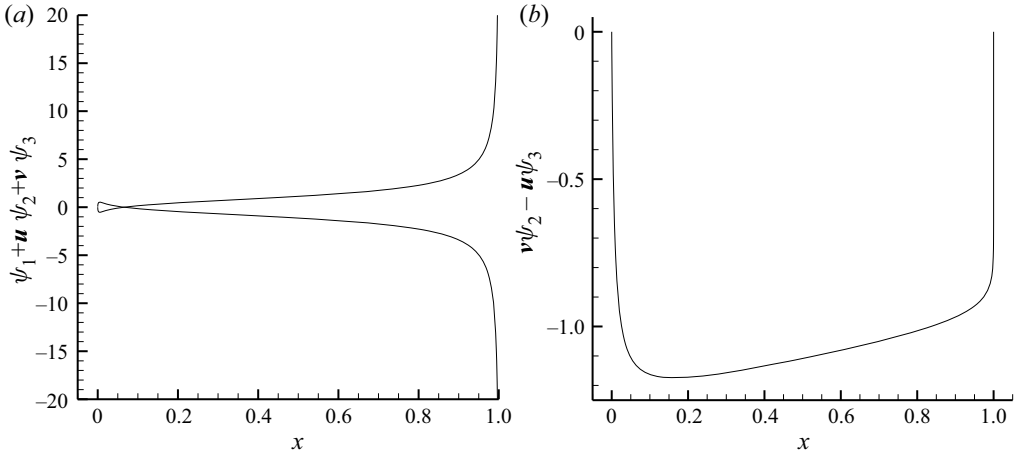


Figure 24. (*a*) $I^{(1)} = \psi_1 + \boldsymbol{v} \cdot (\psi_2, \psi_3)$ and (*b*) $I^{(2)} = v\psi_2 - u\psi_3$ on the airfoil profile computed with the analytic lift-based adjoint solution for incompressible, inviscid flow at $\alpha = 0°$ past a van de Vooren airfoil with trailing-edge angle $\tau = 16°$ and 12 % thickness.

as long as they are not orthogonal to the flow. However, numerical compressible adjoint solutions do show singularities along the incoming stagnation streamline (Giles & Pierce 1997; Peter *et al.* 2022), at the trailing edge/rear stagnation point (Giles & Pierce 1997; Lozano 2018, 2019*b*; Peter *et al.* 2022) and at walls (in the form of mesh-diverging adjoint solutions) (Lozano 2019*b*; Peter *et al.* 2022), which are the analogue of the singularities found in incompressible flow, but also along certain supersonic characteristics (Lozano 2018; Peter *et al.* 2022) without an analogue in the incompressible case. The former singularities are likely governed by a mechanism similar to the one described in this paper (this has already been proven for the incoming stagnation streamline in Giles & Pierce 1997), and probably with the same exponents, at least for subsonic flows.

Giles and Pierce's seminal work (Giles & Pierce 2001) has just turned 20 years old. We would like to finish by quoting their closing remarks, which are still as valid today as they were then: 'An improved understanding of the behavior of adjoint solutions is necessary both to rigorously establish the theoretical basis for engineering optimal design methods and to illuminate the role of the adjoint solution in numerical error analysis. (...) Future developments along these lines will lead to great improvements in accuracy for key engineering quantities such as lift and drag.' We could not agree more.

Funding. The research described in this paper has been supported by INTA and the Ministry of Defence of Spain under grants Termofluidodinámica (IGB99001) and IDATEC (IGB21001).

Declaration of interests. The authors report no conflict of interest.

Author ORCIDs.
Carlos Lozano https://orcid.org/0000-0001-9449-0466.

References

Anderson, W.K. & Venkatakrishnan, V. 1999 Aerodynamic design optimization on unstructured grids with a continuous adjoint formulation. *Comput. Fluids* **28**, 443–480.

Baeza, A., Castro, C., Palacios, F. & Zuazua, E. 2009 2-D Euler shape design on nonregular flows using adjoint Rankine-Hugoniot relations. *AIAA J.* **47** (3), 552–562.

https://doi.org/10.1017/jfm.2022.415 Published online by Cambridge University Press

CASTRO, C., LOZANO, C., PALACIOS, F. & ZUAZUA, E. September 2007 Systematic continuous adjoint approach to viscous aerodynamic design on unstructured grids. *AIAA J.* **45** (9), 2125–2139.

CHADWICK, E., CHRISTIAN, J.M., KAPOULAS, A. & CHALASANI, K. 2019 The theory and application of Eulerlets. *Phys. Fluids* **31**, 047106.

DELFOUR, M.C. & ZOLÉSIO, J.-P. 2011 *Shape and Geometries: Analysis, Differential Calculus and Optimization*, 2nd edn. SIAM.

EMANUEL, G. 2000 *Analytical Fluid Dynamics*, 2nd edn (chapter 5.7). CRC Press.

FIDKOWSKI, K. & DARMOFAL, D. 2011 Review of output-based error estimation and mesh adaptation in computational fluid dynamics. *AIAA J.* **49** (4), 673–694.

FIDKOWSKI, K.J. & ROE, P.L. 2010 An entropy adjoint approach to mesh refinement. *SIAM J. Sci. Comput.* **32** (3), 1261–1287.

GILES, M.B., DUTA, M.C., MÜLLER, J.-D. & PIERCE, N.A. 2003 Algorithm developments for discrete adjoint methods. *AIAA J.* **41** (2), 198–205.

GILES, M. & HAIMES, R. 1990 Advanced interactive visualization for CFD. *Comput. Syst. Engng* **1** (1), 51–62.

GILES, M.B. & PIERCE, N.A. 1997 Adjoint equations in CFD: duality, boundary conditions and solution behavior. *AIAA Paper* 97-1850.

GILES, M.B. & PIERCE, N.A. 1998 On the properties of solutions of the adjoint Euler equations. In *Numerical Methods for Fluid Dynamics VI* (ed. M. Baines). ICFD.

GILES, M. & PIERCE, N. 1999 Improved lift and drag estimates using adjoint Euler equations. *AIAA Paper* 99-3293.

GILES, M. & PIERCE, N. 2000 An introduction to the adjoint approach to design. *Flow Turbul. Combust.* **65** (3), 393–415.

GILES, M.B. & PIERCE, N.A. 2001 Analytic adjoint solutions for the quasi-one-dimensional Euler equations. *J. Fluid Mech.* **426**, 327–345.

GILES, M.B. & PIERCE, N.A. 2002 Adjoint error correction for integral outputs. In *Error Estimation and Solution Adaptive Discretization in Computational Fluid Dynamics* (ed. T. Barth & H. Deconinck), Lecture Notes in Computer Science and Engineering, vol. 25, pp. 47–95. Springer Verlag.

JAMESON, A. 1988 Aerodynamic design via control theory. *J. Sci. Comput.* **3** (3), 233–260.

KATZ, J. & PLOTKIN, A. 2001 *Low Speed Aerodynamics*, 2nd edn. Cambridge University Press.

KAVVADIAS, I., PAPOUTSIS-KIACHAGIAS, E. & GIANNAKOGLOU, K. 2015 On the proper treatment of grid sensitivities in continuous adjoint methods for shape optimization. *J. Comput. Phys.* **301**, 1–18.

KENWAY, G.K., MADER, C.A., HE, P. & MARTINS, J.R. 2019 Effective adjoint approaches for computational fluid dynamics. *Prog. Aerosp. Sci.* **110**, 100542.

KROGER, J., KUHL, N. & RUNG, T. 2018 Adjoint volume-of-fluid approaches for the hydrodynamic optimisation of ships. *Ship Technol. Res.* **65** (1), 47–68.

KÜHL, N., MÜLLER, P. & RUNG, T. 2021 Continuous adjoint complement to the Blasius equation. *Phys. Fluids* **33** (3), 033608.

LOZANO, C. 2012 Discrete surprises in the computation of sensitivities from boundary integrals in the continuous adjoint approach to inviscid aerodynamic shape optimization. *Comput. Fluids* **56**, 118–127.

LOZANO, C. 2017 On mesh sensitivities and boundary formulas for discrete adjoint-based gradients in inviscid aerodynamic shape optimization. *J. Comput. Phys.* **346**, 403–436.

LOZANO, C. 2018 Singular and discontinuous solutions of the adjoint Euler equations. *AIAA J.* **56** (11), 4437–4452.

LOZANO, C. 2019*a* Entropy and adjoint methods. *J. Sci. Comput.* **81**, 2447–2483.

LOZANO, C. 2019*b* Watch your adjoints! Lack of mesh convergence in inviscid adjoint solutions. *AIAA J.* **57** (9), 3991–4006.

LOZANO, C. & PONSIN, J. 2012 Remarks on the numerical solution of the adjoint quasi-one-dimensional Euler equations. *Intl J. Numer. Meth. Fluids* **69** (5), 966–982.

LOZANO, C. & PONSIN, J. 2021*a* Exact inviscid drag-adjoint solution for subcritical flows. *AIAA J.* **59** (12), 5369–5373.

LOZANO, C. & PONSIN, J. 2021*b* On the mesh divergence of inviscid adjoint solutions. WCCM-ECCOMAS2020 (ed. F. Chinesta, R. Abgrall, O. Allix & M. Kaliske). Scipedia. doi:10.23967/wccm-eccomas.2020.258.

LOZANO, C. & PONSIN, J. 2022 Singularity and mesh divergence of inviscid adjoint solutions at solid walls. arXiv:2201.08129.

LUCHINI, P. & BOTTARO, A. 2014 Adjoint equations in stability analysis. *Annu. Rev. Fluid Mech.* **46**, 493–517.

MARTA, A.C., SHANKARAN, S., WANG, Q. & VENUGOPAL, P. 2013 Interpretation of adjoint solutions for turbomachinery flows. *AIAA J.* **51** (7), 1733–1744.

MILNE-THOMSON, L.M. 1962 *Theoretical Hydrodynamics*, 4th edn. Macmillan.

https://doi.org/10.1017/jfm.2022.415 Published online by Cambridge University Press

NADARAJAH, S. & JAMESON, A. 2000 A comparison of the continuous and discrete adjoint approach to automatic aerodynamic optimization. *AIAA Paper* 2000-0667.

OTHMER, C. 2014 Adjoint methods for car aerodynamics. *J. Math. Indus.* **4** (1), 6.

PETER, J. & DWIGHT, R.P. 2010 Numerical sensitivity analysis for aerodynamic optimization: a survey of approaches. *Comput. Fluids* **39** (10), 373–391.

PETER, J., RENAC, F. & LABBÉ, C. 2022 Analysis of finite-volume discrete adjoint fields for two-dimensional compressible Euler flows. *J. Comput. Phys.* **449**, 110811.

VENDITTI, D.A. & DARMOFAL, D.L. 2002 Grid adaptation for functional outputs: application to two-dimensional inviscid flows. *J. Comput. Phys.* **176**, 40–69.

https://doi.org/10.1017/jfm.2022.415 Published online by Cambridge University Press